Draft version November 18, 2025
Typeset using LaTeX default style in AASTeX7.0.1

JWST View of the Supernebula in NGC 5253. II. Nebular Lines.

Sara C. Beck [1], Jean L. Turner [2], Elm Zweig [3], John H. Black [4], Paul T. P. Ho [5], David S. Meier [6], Sergiy Silich [7], Daniel P. Cohen [3], S. Michelle Consiglio [3], and Nicholas G. Ferraro [3]

[1] School of Physics and Astronomy, Tel Aviv University
[2] Department of Physics and Astronomy, UCLA
[3] UCLA Department of Physics and Astronomy
[4] Chalmers Institute of Technology
[5] Academia Sinica Astronomy and Astrophysics
[6] New Mexico Institute of Mining and Technology
[7] Instituto Nacional de Astrofísica Óptica y Electrónica

ABSTRACT

The nearby dwarf starburst NGC 5253 is dominated by a compact radio-infrared supernebula powered by a very young and bright embedded Super Star Cluster (SSC) of $\sim 10^9 L_\odot$. We observed this source and its surroundings over the 5-25μm range with MIRI/MRS on JWST and in Paper I (Turner et al. 2025) presented the JWST view of the region and its continuum features. We now present the more than 70 emission lines of HI, H_2 and metal ions detected by MIRI/MRS. We derive the extinction by comparing HI recombination to the free-free radio continuum and find that it is very flat, i.e., almost independent of wavelength, over this spectral range. Nebular conditions are consistent with young ($\lesssim 5 \times 10^6$ years) and very massive stars. All regions show high excitation, but the spatial distribution of the high excitation lines suggests that photons with energies close to 50eV are escaping the supernebula core in spite of 35 magnitudes of visual extinction.

Keywords: Blue compact dwarf galaxies (165) — starburst galaxies (1570) — infrared spectroscopy (2285) — young massive clusters (2049)—James Webb Space Telescope (2291)

1. INTRODUCTION

This is the second in a series of papers reporting on a project of 5-28μm spectroscopy of the starburst in the nearby (D=3.7 Mpc) dwarf galaxy NGC 5253, carried out with the MIRI/MRS spectrometer on JWST. In Paper 1 (Turner et al. 2025) the data reduction and analysis are described in detail and the main features of the infrared continuum are discussed. In this paper we present the rich variety of emission lines that dominate the mid-infrared spectra and analyze the overall picture of extinction, temperature, and ionization in the starburst. A future paper (Zweig et al, in preparation) will model the ionization in detail.

NGC 5253 is a much-studied and remarkable source. It hosts a complex starburst region with multiple identified star clusters and molecular gas features. The luminosity of the starburst is dominated by an extremely bright radio-infrared supernebula which has total ionizing flux $Q_o \sim 7.7 \times 10^{52}$ s^{-1} (Turner et al. 1998; Rodríguez-Rico et al. 2007; Bendo et al. 2017). The nebula is powered by an embedded star cluster, so deeply obscured as to be undetected at wavelengths shorter than 1.9μm (Turner & Beck 2004; Alonso-Herrero et al. 2004), and with at least $\sim$ 1000 and more likely 5000-7000 O stars (Rodríguez-Rico et al. 2007) within a few cubic parsecs. The starburst is noteworthy because of its location in a low $\sim 0.2 - 0.3 Z_\odot$ metallicity galaxy (Walsh & Roy 1989; Kobulnicky et al. 1997; Monreal-Ibero et al. 2010), its youth (the brightest star cluster is estimated to be less than 1.5 to 3.5 Myr years old, Harris et al. 2004; Alonso-Herrero et al. 2004; Calzetti et al. 2015), and its intensity (Turner & Beck 2004; Alonso-Herrero et al. 2004; Rodríguez-Rico et al. 2007; Bendo et al. 2017; Consiglio et al. 2017). The radiation fields and temperatures in this region must be extreme, approaching conditions in the early Universe. The brightest cluster is a good candidate for a proto-globular, and the galaxy as a whole is a possible Local Universe analogue to starbursts at Cosmic Noon.

The starburst in NGC 5253 is a complex region holding many star clusters, gas and dust features; it has significant obscuration and the optical appearance is strongly affected by extinction. In Paper I we used the new JWST data to map the sources of hot dust continuum emission; the observations and data reduction are discussed in detail in Paper I and are briefly summarized in the next section. From the infrared continuum and other observations we defined four sources of particular interest, which we believe are likely to be young embedded star clusters. The continuum analysis of Paper 1 concentrated on those four regions, which are reviewed in Section 3. Section 3 also introduces the rich emission-line spectrum detected by JWST. In Section 4 we use the HI recombination lines to derive and discuss the extinction to the NGC 5253 starburst. Section 5 introduces the fine-structure emission lines of metal ions that dominate the mid-infrared spectrum and discusses the radiation field that creates them, their role in cooling, and what they suggest about the stellar populations of the embedded star clusters and the escape of photons therefrom.

2. DATA ANALYSIS AND REDUCTION

Reduction and analysis of the JWST data presented many challenges, which are discussed in detail in Paper 1. We review the process here briefly and refer the reader to Paper 1 for details.

A single science pointing of the MIRI/MRS spectrometer and a dedicated background were observed in March 2022 for Program JWST-GO-4302, P.I. J. Turner. Data were obtained for each of the short, medium and long grating settings in all 4 channels of the spectrometer, for a total of 12 bands covering wavelengths 4.98-28μm. The spatial resolution ranges from $FWHM = 0.3''$ at the shortest wavelength to $0.9''$ at the longest, and the spectral resolution from $R = 1300$-3700 (Argyriou et al. 2023a).

NGC 5253 required special approaches to data reduction because of the extreme infrared brightness of the central source, which caused spectral "fringing" so strong that the STSCI defringing routine can not completely remove it. There are also spatial artifacts such as the "petals" of the point spread function and the "cruciform" (Gáspár et al. 2021) that affect nearly the entire field of view. In addition, the background pointing was found to have significant continuum and line emission so we created a custom background for subtraction, which is described in Paper I.

Since defringing is more effective on 1D spectra than 3D cubes, we defined regions to serve as effective apertures for extraction of spectra. The starburst is a combination of compact sources and extended emission, so we use fixed apertures rather than "cones" to analyze fluxes. Following the recommendation that apertures larger than the point spread function be used to compensate for known artifacts in MRS cubes (Law et al. 2023; Argyriou et al. 2023b; Dicken et al. 2024), our apertures have $r \gtrsim 0.8^{''}$, giving a diameter approximately twice the FWHM at $\lambda \sim 20\mu$m, which should render resampling noise negligible (Law et al. 2023). We used these apertures for the regions to extract spectra using in CARTA, by summing intensities using the "SUM" statistic. These intensity sums were converted to Jy using the header parameter, PIXAR, which describes the solid angles of pixels for the individual bands. These converted 1D region spectra were then defringed using the algorithm from jwst.residual_fringe.utils.

Lines were identified by eye in the de-fringed 1D spectra and fit with the Specviz Gaussian procedure to give fluxes, centroids, and errors. Velocity centroids were checked to assure correct line identification. Lines of lower signal-to-noise show more velocity shifts, as expected from the ~ 100 kms^{-1} resolution of the spectrometer, but even these were typically within 10-15 kms^{-1} of the expected velocity of NGC 5253. The greatest source of uncertainty in the line fluxes is definition of the underlying continuum baseline, which is often affected by residual fringing. For nearly all lines the default Specviz "surroundings" baseline was used. For a limited number of closely spaced lines, we defined a custom baseline. We estimated the uncertainty by duplicating the Gaussian fit with the same bandwidth and baseline-subtraction parameters on a nearby line-free section of continuum. While we did not use the cubes for fitting spectra due to the fringing, we note that the uncertainties given by Cubeviz and by Gaussian fit routines in CARTA for the line fits are typically smaller than what we have adopted here. The uncertainties we list for the line fluxes are from the fits and do not include systemics such as baseline, photometric or aperture uncertainties.

We established ICRS coordinates for the cubes by comparing to a high resolution map from the ALMA archive (Project 2017.1.00964.S, P.I. D. Nguyen) of the 1.3 mm continuum, which is free-free emission (Consiglio et al. 2017; Turner et al. 2017). The astrometry is estimated to be good to $\lesssim 50$ mas. Comparisons with radio continuum are estimated to be good to ∼50mas.

For a few lines, continuum-free line images were constructed. For each line, a range of pixels slightly larger than the linewidth was computed on either side of the line using the MOM3 function of CARTA (median), to obtain a continuum intensity image. Line-plus-continuum images were done with the MOM8 function (peak intensity), with the spectral range specified to isolate the line, 3-6 pixels in extent. For high signal-to-noise unresolved lines, the MOM8 images, in units of MJy/sr, will be proportional to the line flux. Continuum images were subtracted from the MOM8 maps to give continuum-free line images.

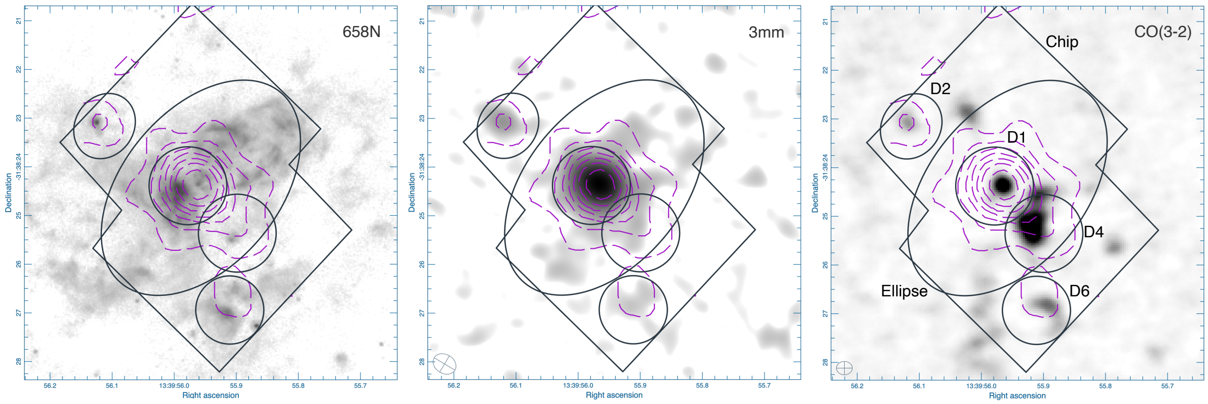

Figure 1. The JWST chip (rectangular outline) and the regions used for spectral extraction are displayed as solid circles and ellipses labeled D1, D2, D4, D6, Ellipse and Chip and overlaid on images of the source at Hα (HST image), 107 GHz ALMA image and the integrated flux of the ALMA CO(3-2) line (ALMA image Turner et al. 2017; Consiglio et al. 2017). Dashed contours trace the $7\mu m$ continuum emission from the JWST MIRI/MRS (Turner et al. 2025).

3. THE HII REGIONS OF THE NGC 5253 STARBURST REGION

In Paper 1 we established the presence of four continuum features within the $\sim$ 120 pc MIRI/MRS footprint. We defined regions NGC 5253-D1, NGC 5253-D2, NGC 5253-D4 and NGC 5253-D6 as effective apertures centered on these mid-IR continuum features, from which spectra were extracted. These regions were defined to be large enough to minimize artifacts and allow defringing. The continuum features and region definitions were discussed in Paper I.

These four continuum regions are displayed in Figure 1, along with maps of the Hα emission from the 656N HST image (Calzetti et al. 1997), the ALMA CO(3-2) image, which measures warm dense molecular gas (Turner et al. 2017; Consiglio et al. 2017), and an ALMA 2.8mm continuum image, which is largely free-free emission. The region names refer to CO clouds identified in (Consiglio et al. 2017), although the JWST apertures are larger than the clouds, $\sim 1\farcs2$-$1\farcs6$ in size, and not centered on them. Two other regions are defined: “Ellipse”, which encompasses the plumes seen in Hα to the northwest and southeast and omits D2 and D6, and “Chip”, which covers the minimum MIRI/MRS footprint at 5μm.

Figure 1 shows that the Hα does not agree well with the strongest radio continuum, which at 3mm is free-free emission. This and other evidence argues that the optical appearance is strongly affected by extinction and that the radio continuum is the more reliable probe of the ionized gas.

The D1, D2, D4 and D6 sources are all associated with molecular gas, ionized gas and dust continuum emission and presumably hold embedded H II regions. Region D1 contains the powerful core of the supernebula, a very strong radio source that dominates the centimeter-wave emission of the starburst. The 7mm radio flux (Rodríguez-Rico et al. 2007) indicates that the region requires an ionization rate of $Q_o \sim 7.7 \times 10^{52} s^{-1}$; 40% of the radio flux emerges from a ~ 5 pc region, which presumably contains the cluster powering the radio core and larger nebula.

This ionization requires $\gtrsim 1000$ O stars within a subarcsecond, pc scale core (Turner & Beck 2004). The star cluster is mixed with hot CO gas (Turner et al. 2017; Consiglio et al. 2017). It is not visible at optical wavelengths (Smith et al. 2020), but the continuum source coincident with the H II region becomes apparent in the near-infrared (Alonso-Herrero et al. 2004; Cohen et al. 2018). In addition to the bright core, there is a Br α source visible in adaptive optics imaging that may be coincident with a faint radio continuum source about $0\farcs25$ to the east of the supernebula core(Cohen et al. 2018); while these JWST MIRI/MRS images do not have the spatial resolution to resolve this feature, it may be related to the bright optical source, Cluster 5 (Calzetti et al. 1997, 2015), directly south and east of the supernebula core. We do not see evidence in the MIR continuum that this is a separate cluster, although the petals of the PSF from D1 would complicate identification if a weaker source were present. It may simply be a denser part of the large scale nebulosity emerging from the supernebula.

While D1 is our primary target, the MIRI/MRS continuum images (Paper I) revealed three more continuum sources, and allow us to determine their separate contributions to the supernebula. D2 is associated with an optical and near-infrared point source and also coincides with a CO feature (Consiglio et al. 2017); a faint Hα point source is visible. D4 is notable because it has the strongest CO emission, and most massive molecular cloud in the region (Consiglio et al. 2017), as well as embedded star formation. D4 is 50 times fainter in the continuum than source D1, but has luminosity of $\sim 10^7$ $L_\odot$, comparable to the giant H II regions W49 or 30 Doradus. Because D4 is $\lesssim 1''$ away (15 pc on the plane of the sky) from D1, it is affected by the spatial artifacts created by D1, including the point spread function (PSF) "petals" and the cruciform artifact. D4 has the worst fringing of all the regions but also the strongest PAH features (Paper I). D4 will be a good case to study possible feedback effects from that very luminous cluster, although it is difficult to study with MIRI/MRS. D6 is a more diffuse region of radio continuum and CO emission region located ∼ 50pc to the southwest of D1. Its H II region appears as a point-like Paα source (Alonso-Herrero et al. 2004); we associate D6 with Cluster 24 of Harris et al. (2004). Two additional regions were added. "Chip" corresponds to the 5μm footprint, the smallest of the 12 spectral bands and the spatial region common to them all. The "Ellipse" encompasses the plumes to the northwest and southeast of the central source apparent in the Hα image of Figure 1, and we henceforth refer to these Hα features as "the plumes".

3.1. *Mid-Infrared Emission Lines*

In addition to strong continuum emission (Turner et al. 2025), JWST-MIRI/MRS detected more than seventy ionic and molecular emission lines in the 5-25μm spectra of NGC 5253. We have extracted line fluxes for each of the apertures corresponding to the four H II regions, D1, D2, D4, D6, the "Ellipse" and "Chip" (Fig. 1). Line fluxes for the regions are presented in Table 1. The wealth of identified lines is due in part to the weakness of PAH features in this source. Velocity centroids determined from the Gaussian fits for the lines are also given, and were used to verify the line identifications; lower signal-to-noise lines can show a shift of 10-20 km s^{-1}, since the resolution is 80-200 km s^{-1}. The lines are for the most part unresolved. There are 7 lines that have not yet been identified; their observed wavelengths are not consistent with any known ion at the velocity of NGC 5253. These appear in the table as "UIL".

There are three types of emission line detected: recombination lines of HI, fine-structure lines of metal ions, and the pure rotational lines of H_2. The HI recombination lines are produced in the ionized gas of H II regions. They have been extensively studied over the years and their behaviour calculated for a very wide range of possible nebular conditions. There are 29 recombination lines of HI detected, from the Pfund ($n_L = 5$)and Humphreys ($n_L = 6$) series, as well as lines from the $n_L = 7 - 10$ series. In § 4 we use the HI recombination lines to probe the ionization and stellar content of the sources, derive the total extinction, and find how the extinction depends on wavelength in the 5-25μm range.

In §5 we introduce the fine-structure lines of metal ions. The emitting ions are photo-ionized, so their populations depend on the UV spectra of the exciting stars. These are magnetic quadrupole transitions, and therefore "forbidden", and the emitting levels are collisionally excited so these lines can be sensitive to the nebular density, as will be discussed below. The fine-structure lines are crucial for deriving the input ionization that excites the H II region emission.

We discuss briefly the basic picture the JWST data gives of very high excitation and hard ionizing radiation in the starburst; full results from CLOUDY and models of the exciting stellar populations will be presented in future papers, in which the rotational lines of H_2 will also be presented and discussed.

Table 1. Line Fluxes in NGC 5253

		D1		D2		D4		D6		Ellipse	Chip
$\lambda_{\rm rest}$	Line	v^a	Flux^b	v	Flux	v	Flux	v	Flux	Flux	Flux
4.9117	UIL	...	...	376	0.4 (0.1)	374	0.5 (0.2)	...	...	...	...
4.9237	HI 23-7	424	1.5 (0.3)	...	...	...	...	...	...	...	...
4.9709	HI 22-7	341	1.1 (0.3)	433	0.5 (0.1)	...	...	...	380	1.9 (1.0)	...
5.0261	HI 21-7	360	1.2 (.03)	...	...	...	...	...	...	...	...
5.1287	HI 10-6	377	12.9 (0.3)	364	0.8 (0.1)	383	1.5 (0.1)	366	1.1 (0.20)	20.5 (1.0)	25.5 (1.0)
5.1693	HI 19-7	357	1.0 (0.3)	...	...	...	...	...	...	...	...
5.2637	HI 18-7	393	1.0 (0.3)	...	...	354	0.4 (0.1)	...	...	2.7 (1.0)	...
5.2970	UIL	...	...	...	...	...	...	402	1.2 (0.30)	...	...
5.3402	[Fe II]	394	9.7 (0.2)	395	1.5 (0.2)	382	4.0 (0.1)	393	3.0 (0.30)	28.1 (1.0)	44.0 (1.0)
5.3798	HI 17-7	382	1.8 (0.2)	...	...	...	...	...	...	3.3 (0.5)	...
5.5112	H_2 S(7)	384	1.0 (0.2)	...	...	...	...	425	0.3 (0.1)	1.9 (0.5)	3.0 (1.0)
5.5252	HI 16-7	378	1.6 (0.2)	...	...	...	...	...	...	4.1 (1.0)	...

Table 1 *continued on next page*

Table 1 *(continued)*

		D1		D2		D4		D6		Ellipse	Chip
$\lambda_{\rm rest}$	Line	v^a	Flux[b]	v	Flux	v	Flux	v	Flux	Flux	Flux
5.7115	HI 15-7	349	2.2 (0.3)	...	...	...	...	...	...	3.4 (1.0)	2.9 (1.5)
5.9082	HI 9-6	378	19.6 (0.5)	382	0.8 (0.5)	406	1.6 (0.1)	406	1.2 (0.20)	27.4 (1.0)	32.7 (2.0)
5.9568	HI 14-7	391	3.5 (0.5)	...	...	...	...	...	...	5.3 (1.0)	6.3 (2.0)
5.9820	[K IV]	410	4.8 (0.5)	...	...	...	...	...	...	6.3 (1.0)	7.9 (2.0)
6.2919	HI 13-7	361	3.8 (0.5)	...	...	...	...	...	...	7.1 (1.0)	8.4 (2.0)
6.6366	[Ni II]	373	4.0 (0.5)	...	...	...	...	...	...	3.9 (1.0)	...
6.7720	HI 12-7	367	4.8 (0.5)	415	0.2 (0.2)	383	0.3 (0.05)	414	0.3 (0.05)	7.1 (1.0)	7.9 (0.5)
6.9095	H_2 S(5)	385	3.5 (0.5)	398	0.6 (0.1)	414	1.3 (0.2)	402	0.4 (0.10)	5.7 (1.0)	6.6 (1.0)
6.9853	[Ar II]	381	25.3 (0.5)	390	2.7 (0.3)	393	6.6 (0.2)	405	4.7 (0.20)	56.6 (1.0)	78.1 (1.0)
7.3177	[Na III]	383	13.6 (0.3)	...	...	355	0.9 (0.4)	...	...	17.4 (1.0)	20.1 (1.0)
7.4599	HI 6-5	379	108 (0.3)	388	4.9 (0.2)	379	11.2 (0.4)	401	7.4 (0.10)	156 (1.0)	183 (2.0)
7.5025	HI 8-6	384	30.0(.3)	380	1.8 (0.2)	392	3.2 (0.4)	403	2.4 (0.10)	43.8 (2.0)	48.8 (2.0)
7.5081	HI 11-7	394	8.0(0.3)	395	0.4 (0.4)	375	0.8 (0.4)	403	0.6 (0.10)	11.5 (2.0)	12.7 (2.0)
7.7804	HI 16-8	...	...	...	...	...	...	...	...	3.0 (1.0)	...
8.1549	HI 15-8	380	3.0 (0.4)	...	...	...	...	...	...	1.4 (0.5)	2.0 (1.0)
8.4095	C I	369	3.0 (0.4)	...	...	395	0.4 (0.2)	...	...	4.4 (0.5)	6.3 (0.5)
8.6645	HI 14-8	...	...	...	...	...	...	391	0.2 (0.20)	2.2 (1.0)	...
8.7601	HI 10-7	384	7.2 (0.4)	404	0.3 (0.1)	395	0.7 (0.1)	421	0.5 (0.10)	12.4 (0.5)	13.5 (1.0)
8.9914	[Ar III]	380	270 (0.4)	383	13.2 (0.1)	384	40.6 (0.1)	398	27.4 (0.10)	471 (1.0)	569 (1.0)
9.0995	UIL	...	...	379	0.8 (0.1)	391	1.1 (0.1)	397	0.7 (0.10)	7.3 (1.0)	14.8 (0.5)
9.3920	HI 13-8	372	0.9 (0.3)	...	...	...	...	...	...	2.0 (0.5)	...
9.6649	H_2 S(3)	383	1.2 (0.3)	375	0.4 (0.1)	392	1.6 (0.2)	397	0.8 (0.10)	5.7 (0.5)	8.6 (1.0)
10.5105	[S IV]	376	2112 (0.2)	366	48.7 (0.2)	373	221 (0.1)	396	94.9 (0.10)	3324 (1.0)	3691 (0.5)
10.7690	UIL	391	1.1 (0.2)	...	...	...	...	...	...	...	...
11.3087	HI 9-7	394	2.0 (0.2)	369	0.5 (0.1)	379	1.1 (0.1)	395	0.6 (0.20)	15.2 (1.0)	18.9 (2.0)
11.7619	[Cl IV]	400	3.1 (0.5)	...	...	391	0.4 (0.2)	396	0.2 (0.05)	3.6 (3.0)	7.0 (1.0)
12.2790	H_2 S(2)	...	...	377	0.3 (0.1)	385	1.5 (0.1)	387	0.5 (0.02)	3.6 (1.0)	5.6 (0.5)
12.3719	HI 7-6	382	35.3 (0.6)	389	1.6 (0.1)	383	5.8 (0.1)	397	2.6 (0.05)	59.7 (2.0)	72.2 (1.0)
12.3887	HI 11-8	381	4.2 (0.6)	396	0.2 (0.1)	384	0.9 (0.1)	375	0.3 (0.05)	7.5 (2.0)	9.8 (1.0)
12.5871	HI 14-9	381	3.1 (0.6)	...	...	...	...	...	...	...	3.6 (1.0)
12.8136	[Ne II]	390	136 (0.6)	400	14.7 (0.1)	400	41.1 (0.1)	406	27.7 (0.02)	301 (4.0)	409 (1.0)
13.4645	UIL	...	...	387	0.3 (0.1)	395	1.2 (0.7)	395	0.2 (0.03)	...	...
14.1830	HI 13-9	370	1.6 (0.5)	...	...	...	...	394	0.1 (0.01)	3.9 (1.0)	4.1 (1.0)
14.3182	UIL	372	2.3 (0.5)	...	...	414	0.4 (0.2)	...	...	2.5 (1.0)	3.2 (1.0)
14.3678	[Cl II]	...	...	389	0.1 (0.02)	...	...	401	0.1 (0.02)	...	...
15.5551	[Ne III]	404	1350 (0.5)	411	75.7 (0.1)	409	340 (0.4)	432	131 (0.05)	2673 (3.0)	3222 (5.0)
16.2091	HI 10-8	368	4.8 (0.5)	383	0.4 (0.1)	375	1.1 (0.2)	387	0.5 (0.02)	7.3 (2.0)	10.4 (1.0)
16.8806	HI 12-9	...	...	390	0.1 (0.1)	...	...	397	0.2 (0.02)	3.3 (1.0)	...
17.0348	H_2 S(1)	391	2.8 (0.7)	391	0.4 (0.1)	397	2.0 (0.1)	399	0.7 (0.02)	7.1 (1.0)	11.4 (0.3)
17.8855	[P III]	349	5.1 (0.5)	403	0.4 (0.1)	402	1.4 (0.1)	415	1.2 (0.05)	11.8 (1.0)	13.6 (0.3)
17.9360	Fe II	393	8.6 (0.5)	401	0.5 (0.1)	356	1.6 (0.1)	393	0.6 (0.05)	13.8 (1.0)	16.6 (0.3)
18.7130	[S III]	380	490 (3.0)	384	38.9 (0.1)	387	139 (0.2)	395	81.3 (0.10)	1202 (2.0)	1516 (2.0)
18.7930	UIL	...	...	...	...	...	...	...	...	...	5.1 (1.0)
19.0619	HI 8-7	376	15.1 (1.0)	375	0.8 (0.1)	396	2.8 (0.2)	396	0.9 (0.10)	30.9 (2.0)	31.9 (2.0)
21.8302	[Ar III]	370	9.0 (3.0)	442	0.8 (0.1)	392	2.7 (0.1)	396	1.4 (0.03)	23.4 (2.0)	28.5 (2.0)
21.9550	He I	366	8.9 (3.0)	...	...	...	...	...	...	11.3 (2.0)	8.7 (2.0)
22.3404	HI 11-9/13-10	...	...	...	...	...	...	...	...	6.9 (3.0)	7.1 (2.0)
22.9250	[Fe III]	377	13.7 (3.0)	421	1.9 (0.1)	455	4.3 (0.3)	441	2.7 (0.20)	38.0 (1.0)	51.8 (1.0)
24.7438	[F I]	...	...	...	...	...	...	400	0.6 (0.10)	...	...
25.8903	[O IV]	325	8.7 (2.0)	...	...	438	2.5 (0.5)	394	0.9 (0.20)	19.8 (6.0)	30.1 (5.0)
25.9884	[Fe II]	374	15.7 (2.0)	377	1.4 (0.2)	401	3.8 (0.5)	411	1.8 (0.20)	29.1 (6.0)	45.7 (5.0)

Table 1 *continued on next page*

Table 1 *(continued)*

		D1		D2		D4		D6		Ellipse	Chip
$\lambda_{\rm rest}$	Line	v^a	Flux^b	v	Flux	v	Flux	v	Flux	Flux	Flux

Note—[a] Velocity centroids for lines are in km s^{-1}. [b] Units of flux are 10^{-18} W m^{-2}. Uncertainties are in line fluxes are determined from fluxes in adjacent line-free continuum, see text. They do not include aperture correction or absolute flux calibration uncertainties. For lines much stronger than adjacent continuum, fluxes here are quoted to 1% but the absolute fluxes are uncertain to the 4% photometric uncertainty of MIRI-MRS.

4. EXTINCTION LAW IN THE MID-INFRARED

The NGC 5253 starburst is deeply embedded and obscured even in the mid-infrared. The dominant star formation site in D1 is immersed within a CO cloud (Turner et al. 2017) and is so completely obscured at wavelengths shorter than 2.2μm (Alonso-Herrero et al. 2004) that no stellar features are seen. Only the dusty compact H II region excited by the O stars is observable, and even that is only fully revealed at radio wavelengths (Beck et al. 1996; Calzetti et al. 1997). D2, D4 and D6 are also closely associated with molecular gas. We must therefore correct for the extinction if we are to understand the embedded stars.

The study of infrared extinction has until now largely concentrated on the H, J, and K bands, and has mostly depended on observing stars of known color index and spectral type on different sightlines through the ISM. This method is limited in NGC 5253, because it requires sightlines to individual stars, which cannot be done here. Moreover the sources in NGC 5253 appear to be so deeply embedded that they cannot be seen shortward of J. Using reddening to get extinction is also problematic: in NGC 5253 the Balmer line ratios suggest visual extinctions of $A_V \sim 1-2$ (Walsh & Roy 1989; Monreal-Ibero et al. 2010), while the infrared recombination lines suggest that visual extinctions are at least $A_v \sim 15$ (Turner et al. 2003; Alonso-Herrero et al. 2004; Martín-Hernández et al. 2005). The only way to ensure a reliable extinction is to use an extinction-free measure of ionized gas, such as radio emission.

The JWST data makes it possible to analyse the interstellar extinction over an unprecedented range of wavelengths, as well as determining if and how it varies spatially over the starburst. We use the HI recombination lines of Table 2 to derive the extinction by comparing to radio free-free. NGC 5253 is a good site for this method because the solid state features such as PAHs (Turner et al. 2025) are relatively weak, making it easier to detect the HI recombination lines. Table 2 shows the 30 recombination lines detected; they arise from four different series and cover the wavelength range from 4.9-22μm. While some of these lines are weak, the suite of HI lines allow us to determine both the total extinction and its variation with wavelength for the different regions. The technique is reviewed in the next section and the results for the individual regions presented in 4.2.1 and 4.2.2.

4.1. *Calculating Extinction from HI lines and Radio Flux*

We establish the interstellar extinction by comparing the HI recombination lines in the JWST spectra to the free-free radio emission measured at 107 GHz, which is not affected by extinction. Simple HII regions have free-free emission that is optically thick ($\propto \nu^{-2}$) at low frequencies and transitions to optically thin ($\propto \nu^{-0.1}$) at a turnover frequency determined by the emission measure $EM = \int n_e^2\, d\ell$. For moderate ($EM \sim 10^4$ cm^{-6}pc) emission measures, typical of evolved HII regions, the emission becomes thin at frequencies higher than $\sim$ 1 GHz (λ = 20 cm). The emission measure in D1 is high, ($EM \gtrsim 10^8$ cm^{-6}pc) (Beck et al. 1996; Turner & Beck 2004), and the overall spectrum of D1 suggests that it is optically thin only at frequencies beyond ∼20 GHz (∼ 1cm, Meier et al. 2002; Turner & Beck 2004; Rodríguez-Rico et al. 2007).

We therefore rely on ALMA maps at 107 GHz (ALMA Project 2013.1.00833.S, P.I. E. Rosolovsky) for our derivation of N_{lyc} for the regions. At this frequency non-thermal radiation is negligible and there is no possibility of dust continuum emission or synchrotron emission in this source; the radio spectrum indicates that the flux is entirely optically-thin free-free emission, which for an ionization-bounded nebula reflects N_{lyc}. The 107 GHz beam is 0.45″, which is smaller than our aperture sizes, and the largest angular scale detected by the interferometer is larger than the MIRI/MRS footprint. Since the JWST cubes were aligned to high resolution 1.3mm ALMA images (§2, Turner et al. 2025), we use the same WCS regions for both radio and infrared.

The strength of an HI recombination line and of the thermal radio (free-free) continuum are linked. Integrated over the volume of an H II region they both depend on the Lyman continuum flux, N_{lyc}. For an ionization-bounded, pure

H nebula, and case B recombination, the flux of an emission line between the upper and lower levels u, l is given by

$$\frac{S_{line}}{\text{erg s}^{-1}\text{cm}^{-2}} = 8.33 \times 10^{-51} \frac{N_{lyc}}{D^2_{Mpc}} \Big(\frac{\varepsilon(u \rightarrow\ l)}{\alpha_B}\Big)$$

where $\varepsilon(u \rightarrow l)$ is the emissivity and α_B the case B recombination coefficient, with line emissivities from (Storey & Hummer 1995). The thermal radio emission S_ν depends on N_{lyc} as

$$\Big(\frac{S_{100}}{\text{mJy}}\Big) = 7.604 \times 10^{-51}\ T_4^{0.507} \nu_{11}^{-0.118} \Big(\frac{n_p}{n_e}\Big) D^{-2}_{Mpc}\ \Big(\frac{N_{lyc}}{s^{-1}}\Big)$$

where T_4 is temperature in units of 10^4 K, and ν_{11} is frequency in units of 100 GHz. The temperature and frequency dependence in the formula for the radio emission arise from the Gaunt factor in the expression for free-free τ and the temperature dependence of α_B (Draine 2011a,b). For $T = 10^4$ K, the ratio of line to free-free flux simplifies to $(S_{line}/10^{-18}\ \text{W}\,\text{m}^{-2}) = 0.427\ em_{28}\ S_{100GHz}(\text{mJy})$, where em_{28} is the emissivity in units of 10^{-28} erg s^{-2} cm^{-3}. The line emissivities depend on temperature as $T_4^{-1.2}$ for IR lines and are relatively insensitive to density. Optical spectroscopy of NGC 5253 (Walsh & Roy 1989; Kobulnicky et al. 1997; López-Sánchez et al. 2007; Monreal-Ibero et al. 2012) indicates temperatures of 9700-12100K. We adopt $T_e = 10^4$ K, within the range of computed T_e (Guseva et al. 2011). Considering that the free-free and recombination lines tend to arise in gas that is slightly cooler than the forbidden lines, we estimate that the uncertainty due to temperature in the ratio is $\lesssim$ 3-4%. Table 2 gives the $\varepsilon(u \rightarrow l)$ for the HI lines in the JWST data set.

Table 2 gives the HI line fluxes for all lines detected at the 2σ level or stronger for each of the D1, D2, D4, D6 sources and for the Ellipse and Chip regions. The radio flux for each region is listed in Table 2, as are the emissivities for reference temperature $T_e = 10^4 K$ and electron density $n_e = 10^4 cm^{-3}$ for each line. We compute the extinction from the observed line strength to that predicted by the radio emission using the equation given.

We take uncertainties in the line strengths from Table 1, and for the ALMA measurements, adopt the standard photometric accuracy of 5% (Argyriou et al. 2023a). The formal errors in the MIR line fluxes based on the Gaussian fits are in many cases much less than the systemic uncertainties that dominate much of the spectrum. While the photometric accuracy and reproducibility of the system is estimated to be 2-6% (Argyriou et al. 2023a; Law et al. 2023), uncertainties in the baselines assumed for the line fits are generally larger and difficult to characterize. Fringing can vary both spatially and spectrally; while the spectra have been defringed, fringes are still present and can affect the baseline, although this should wash out statistically for many lines. There is also the presence of weak PAH emission, which affects mostly the HI 9-7 line at 11.3μm. Fringing, instrumental response, and baseline effects, which are related, are likely to dominate the uncertainties in the line fluxes, in different proportion for each line.

Because the uncertainties are systematic, but in large part independent from line to line, we can use the ensemble of lines to fit the extinction across the band, assuming that it varies relatively smoothly. We do a linear model in R for the variation of apparent extinction, $A(\lambda) = a + b\lambda$. Points above signal-to-noise of 10 were assigned a weight of 1; although the formal S/N of the line fluxes in a relative sense may be higher than 10, we are doing a ratio of JWST and ALMA fluxes and therefore must sum their absolute photometric accuracies, which we estimate at $\sim 5\%$ each. Points below S/N=10 were weighted as $1/SN^2$. We redid the fits with uniform weighting and the results were indistinguishable.

In Figure 2 we show the apparent extinction, derived from the observed and radio-predicted fluxes as $A^{app} = -2.5 \log(S^{obs}/S^{pred})$, for each point. The best fit linear model is shown. The plots show that the mid-infrared extinction for all the NGC 5253 sources is flat with wavelength, as is the case in the Galaxy (Gordon et al. 2023) and other galaxies (e.g. Lai et al. 2024, 2025) D1 has a small positive slope of $0.02 \pm .008$ at the 95% confidence level; for all other regions the fitted slopes are consistent with zero.

Since the extinction is flat, each region can be characterized by a single value for the extinction over the $5.9\mu m$ to $19.1\mu m$ range as A(5-19μm) or $A(MIR)$. We display in each frame the absolute extinction at 14μm, a wavelength chosen as representative because it is in the middle of the observed range and relatively free of solid state features. D1 has the highest extinction across the wavelength range, $A(MIR) = 1.41 \pm 0.19$; D2 has slightly lower extinction of $A(MIR) = 0.73 \pm 0.16$. D4 and D6 are consistent with zero MIR extinction, with $A(MIR) = -0.15 \pm 0.45$ for D4, and $A(MIR) = -0.12 \pm 0.25$ for D6. D4 has the greatest scatter of ~ 0.45 magnitudes, probably due to its proximity to D1, near the cruciform feature and with strong fringing.

It is notable that Ellipse and Chip regions, in which the flux is dominated by D1, have lower extinction than does D1. The apparent extinction or attenuation, $A^{app} = -2.5 \log(S^{obs}/S^{pred})$, is a lower limit to the "mean" extinction

Table 2. HI Line Fluxes in NGC 5253

Line	λ (μm)	$em_{28}(u \to l)^a$	D1	D2	D4	D6	Ellipse	Chip
			Line Flux (10^{-18} W m^{-2})					
HI 23-7	4.9237	0.214	1.4 ± 0.3	...	...	...	2.5	...
HI 21-7	5.0261	0.244	1.1 ± 0.3	...	...	1.9 ± 1.0	...	...
HI 22-7	5.0261	0.281	1.2 ± 0.3	...	...	...	...	...
HI 10-6 (Huδ)	5.1287	4.10	12.9 ± 0.3	0.8 ± 0.3	1.5 ± 0.1	1.1 ± 0.2	20.5 ± 1	25.5 ± 1
HI 19-7	5.1693	0.382	1.0 ± 0.3	...	...	...	...	
HI 18-7	5.2637	0.452	1.0 ± 0.3	...	0.5 ± 0.1	...	2.7 ± 1	...
HI 17-7	5.3798	0.539	1.8 ± 0.3	...	...	...	3.3 ± 1	...
HI 16-7	5.5252	0.649	1.6 ± 0.3	...	...	...	4.1 ± 1	...
HI 15-7	5.7115	0.792	2.2 ± 0.3	...	...	1.0 ± 0.4	3.4 ± 1	...
HI 9-6 (Huγ)	5.908	5.66	19.6 ± 0.5	0.8 ± 0.5	1.6 ± 0.1	1.2 ± 0.2	27.4 ± 1	32.7 ± 2
HI 14-7	5.9568	0.979	3.5 ± 0.5	...	...	...	5.3 ± 1	...
HI 13-7	6.2919	1.23	3.8 ± 0.5	...	...	...	7.1 ± 1	...
HI 12-7	6.7720	1.57	4.8 ± 0.5	2.0 ± 0.2	0.4 ± 0.2	0.3 ± 0.05	7.1 ± 1	3.2 ± 1
HI 6-5 (Pfα)	7.4599	30.4	108 ± 0.3	4.9 ± 0.2	11.2 ± 0.4	7.4 ± 0.1	156 ± 1	183 ± 2
HI 8-6 (Huβ)	7.5025	8.06	30 ± 0.3	1.3 ± 0.2	3.0 ± 0.4	2.2 ± 0.1	43.8 ± 2	48.8 ± 2
HI 11-7	7.5081	2.05	8.0 ± 0.3	...	1.1 ± 0.4	0.5 ± 0.1	11.5 ± 2	12.7 ± 2
HI 15-8	8.1654	0.555	1.2 ± 0.8	...	...	...	1.4 ± 0.5	2.0 ± 2.0
HI 14-8	8.6645	0.686	...	...	...	...	2.2 ± 1	...
HI 10-7	8.7709	2.73	7.2 ± 0.4	0.3 ± 0.3	0.7 ± 0.1	0.6 ± 0.2	12.4 ± 0.5	13.5 ± 0.1
HI 13-8	9.3920	0.860	2.8 ± 0.3	...	...	...	2.0 ± 0.5	
HI 9-7	11.3231	3.71	9.9 ± 0.5	0.5 ± 0.1	1.1 ± 0.1	0.6 ± 0.2	15.2 ± 1	18.9 ± 2
HI 7-6 (Huα)	12.3880	11.5	35.3 ± 0.6	1.6 ± 0.1	5.8 ± 0.3	2.6 ± 0.05	59.7 ± 2	72.2 ± 1
HI 11-8	12.404	1.42	...	0.2 ± 0.1	0.1 ± 0.1	0.3 ± 0.05	7.5 ± 2	9.1 ± 1
HI 14-9	12.5871	0.497	...	...	...	...	3.4 ± 1	...
HI 13-9	14.201	0.621	1.6 ± 0.5	...	...	$0.1 \pm .01$	3.9 ± 1	4.1 ± 1
HI 10-8	16.2091	1.86	4.8 ± 0.5	0.4 ± 0.1	1.1 ± 0.2	0.5 ± 0.02	7.3 ± 2	10.4 ± 0.4
HI 12-9	16.9025	0.785	...	...	...	...	3.3 ± 1	...
HI 8-7	19.0619	4.98	15.1 ± 1	0.8 ± 0.1	2.8 ± 0.2	0.9 ± 0.1	30.9 ± 2	31.9 ± 2
HI 11-9	22.3404	1.00	...	...	...	...	6.9 ± 3	7.1 ± 1
free-free[b]	2.8mm		27.0 ± 0.27	$0.7 \pm .07$	0.9 ± 0.09	0.5 ± 0.05	30.5 ± 0.31	$32.1 \pm .032$

Note—[a] Emissivities are from (Storey & Hummer 1995), with units (10^{-28} erg s^{-1} cm^3) [b] Free-free fluxes are in units of mJy. The uncertainties in line fluxes in the table are statistical uncertainties due to the Gaussian fits to the lines. Absolute flux uncertainties are dominated by absolute photometric accuracy, apertures and astrometry, estimated to be $\sim$ 10%. Uncertainty in the free-free fluxes are the standard photometric uncertainty for this ALMA band.

across the source (Natta & Panagia 1984). While the regions other than D1 have $< 15\%$ of the total radio flux, they constitute 30% of the observed MIR flux. NGC 5253 is nearby and we can isolate individual H II regions on 15 pc scales; for more distant galaxies, where this is not possible, the effect is enhanced. For NGC 5253, the standard correction for "mixed" extinction overestimates the correction for this relatively simple region consisting of four H II regions combined within the MIRI/MRS footprint.

For region D1, we can extend the analysis of extinction into the near-infrared by adopting fluxes for HI lines found from other high resolution observations. The HST/NICMOS observations of Alonso-Herrero et al. (2004) and the Keck/NICMOS observations of Turner et al. (2003), although slit spectra, have sufficient spatial resolution to isolate D1. Those results, combined with the present findings, are plotted in Figure 3 and show the steep fall-off from the near-infrared that was seen by other studies.

How do these values for extinction compare to other results and what do they say about the starburst environment of NGC 5253? Extensive work in J,K and L bands over the years (e.g. Lebofsky & Rieke 1979; Gordon et al. 2021, 2023; Decleir et al. 2022) has demonstrated that extinction $A(\lambda)$ falls steeply with λ from the visible to $\lambda \sim 4\mu m$ and can be approximated as λ^{-k} for k typically between 1 and 2. For example, the extinction to the Galactic Center, derived like our work from HI recombination lines (Lutz et al. 1998) falls as $\approx \lambda^{-1.75}$ from the visible to $\sim 4\mu$m wavelength. At $\sim 4\mu$m it flattens out to be near constant as λ increases until the silicate feature at 9.7μm. Indebetouw et al. (2005) find similar behaviour for GLIMPSE and 2MASS sightlines. The current results, combined with the Brackett line

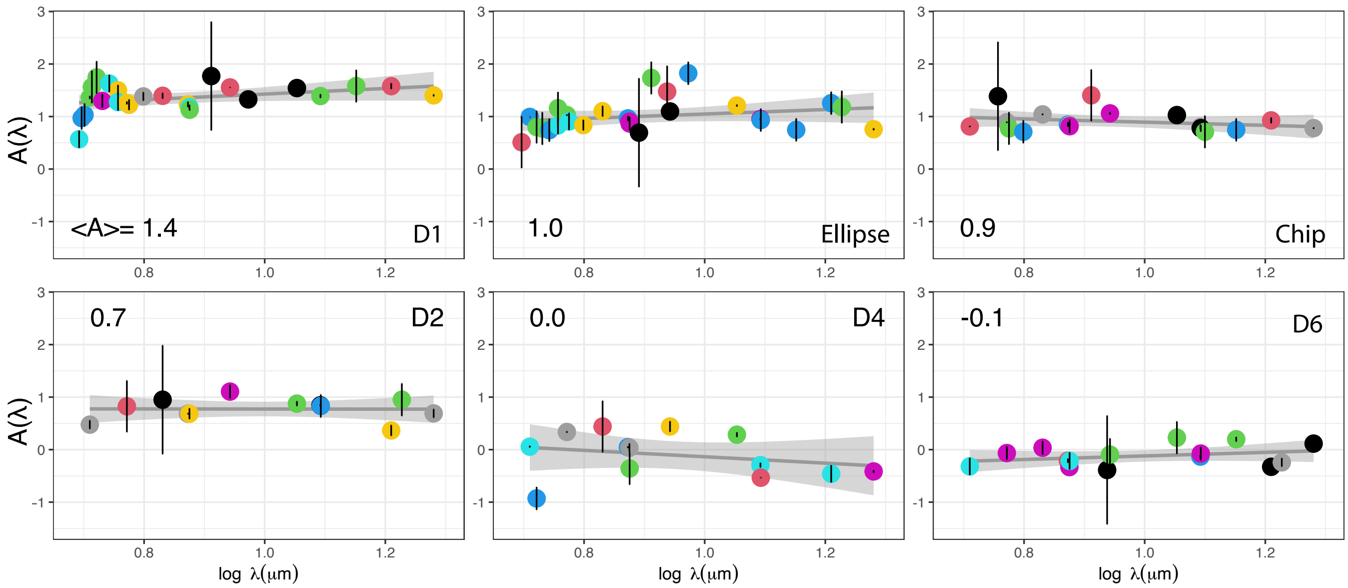

Figure 2. Apparent extinction as determined by the comparison of observed flux to flux predicted from 107 GHz free-free flux. Color is coded to signal-to-noise for each panel, from low (black) to high (pink), and error bars are shown. The best fit linear regression is shown with 95% confidence levels for predictions. The MIRI/MRS datapoints near 5μm in D1 and Ellipse are from high level 7-series lines near the band edge, where instrumental response is degraded.

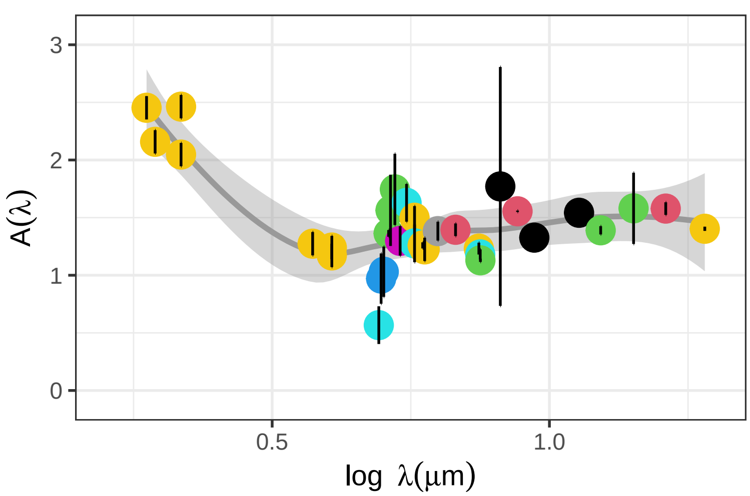

Figure 3. Apparent extinction from the near-infrared to mid-infrared as determined by the comparison of observed flux to flux predicted from 107 GHz free-free flux, including HST and Keck near-infrared fluxes for $\lambda < 5\mu$m (Turner et al. 2003; Alonso-Herrero et al. 2004) as well as JWST MIRI/MRS fluxes. Signal-to-noise is indicated by color from low (black) to high (pink) and error bars. A loess-smoothed fit from R (span 75%) with 95% confidence levels for predictions is shown. The lines around 5μm are from high levels of the n-7 series, which has large scatter due to the instrumental response at the band edge (see Paper 1) creates large scatter in the fluxes.

results of Turner et al. (2003) and Alonso-Herrero et al. (2004), show the same behaviour: there is signficant relative extinction between $Br\gamma$ at 2.17μm and $Br\alpha$ at 4.05μm, while the ratios of $Br\alpha$ 4.05μm and $Pf\alpha$ 7.46μm are close to the theoretical ratio predicted from the radio, indicating negligible relative extinction, or reddening.

There is less known in other sources for the behaviour of extinction at wavelengths longer than $\sim 12\mu m$, but the situation is rapidly changing with JWST. Previous studies find the extinction in the mid-infrared is consistent with flat out through the 19μm HI line excluding the 9.7 and 18μm silicate features Lutz et al. (1996); Chiar & Tielens (2006); Smith et al. (2007); Gordon et al. (2021, 2023). The NGC 5253 result is consistent with the flat extinction curve seen in higher metallicity systems, and has the advantage of being based on the ratio of multiple HI lines to extinction-free radio emission.

Finding that the extinction is near-constant through the JWST wavelength range has the immediate consequence that ratios formed of two lines in this range will be insensitive to extinction. This will be important as we calculate the molecular gas temperature and sketch out the nebular conditions in the following sections of this paper.

4.2. *Extinction to the Individual Regions*

D1 completely dominates the ionization, providing more than 80% of the N_{lyc} in the Chip aperture. Its 1.4 magnitudes of MIR extinction is higher than any other region in the field and is high by any standard, being close to the total extinction to the Galactic Center in the Milky Way. Calzetti et al. (1997) determined a visual extinction of A_V = 9-35 magnitudes from comparing the observed Hα flux to that predicted by the 2 cm free-free fluxes of Beck et al. (1996). The recent extinction curves of Gordon et al. (2023) give A(14μm)/A_V = 0.04, which for our MIR extinction value to D1 of A(MIR) = 1.4 gives A_V = 35 magnitudes, in agreement with the upper bound of Calzetti et al. (1997).

Inferring gas columns for D1 from this number is difficult for such a large extinction. In the Galaxy, the CO column drops off at high extinctions due to ice formation (e.g. Bergin et al. 2002; Pineda et al. 2010), but conditions in D1 are different from Galactic regions. The supernebula core is embedded/mixed with a very bright CO(3-2) source (Turner et al. 2015, 2017). Unusual conditions such as apparently optically thin CO (Consiglio et al. 2017), and high CO temperatures lead to uncertainty in the molecular gas mass of more than an order of magnitude (Turner et al. 2017), It is difficult to infer much about dust or gas columns with current information. It is clear, however, that while line ratios within the MIR are unaffected by reddening, there is still a attenuation of fluxes even in the MIR.

D2 appears in every respect to be a young and obscured young stellar cluster: it appears as a discrete source in radio maps at 15,33, 107 and 230 GHz, is a CO(3-2) and 870μm continuum source and has a weak counterpart in the optical Hα (Fig. 1. We find $A(MIR) = 0.7$ magnitude for D2, implying a visual extinction of $A_V \sim 18$ magnitudes. D2 has the very substantial ionization rate of $1.2 \times 10^{51} s^{-1}$ from the radio flux; at $L \sim 10^7\ L_\odot$, it is comparable to the brightest star formation regions in the Milky Way. Although it has lower extinction than D1, it still falls into the category of "embedded" young clusters with significant MIR extinction. D2 has visible Hα emission, albeit a tiny fraction of what is expected based on its radio luminosity. For these photons to have escaped argues that the extinction in D2, like D1, has a clumpy or porous internal structure.

D4 and D6 are difficult to interpret. Both of them have much lower obscuration than D2 and D1, with infrared extinction formally close to $A(MIR) \sim 0$; given the uncertainties they could have extinctions as high as $A_V \sim 5$ mag. D4 is so close (15 pc) to the dominant D1 cluster as to nearly overlap it in the JWST PSF, and is particularly affected by the cruciform feature. D4 is a very intriguing source; it has some of the strongest CO emission in the field (Fig. 1 as well as the strongest PAH emission (Turner et al. 2025). Therefore it is surprising that the extinction is lower than that of D1 or D2. It may be a blister feature or irradiated by the nearby D1 cluster, or some of the MIR HI flux could be spilling over from D1. D6 is a CO(3-2) and 870μm source associated with [Ne III] and some Hα optical emission. Its radio continuum emission is diffuse, although consistent with a very luminous, $L \sim 10^7\ L_\odot$, star-forming region. The extended and irregular shape of the molecular and continuum emission suggest a fragmentary cloud or filament. It appears to coincide with Harris et al. (2004)'s cluster 24.

4.3. *The Silicate Feature in NGC 5253 Does Not Correlate Simply with the Extinction*

In Galactic HII regions, as well as in many high luminous starburst, AGN and hybrid galaxies, the mid-infrared spectrum has strong absorption features at 9.7μm and 18μm which are attributed to the stretch and bending modes of silicates. These features are detected in the JWST data for the first time in NGC 5253 as shown in the continuum spectra in Figure 4. In Paper 1 we fit the 9.7μm feature in the observed sources following the method of Spoon et al. (2007), and find $\tau_{9.7} = 0.4 \pm 0.1$ in D1. D4 also shows the silicate feature in absorption, weaker than D1 and probably affected by it.

The 9.7μm feature is important as its strength has been observed to correlate with the total obscuration. Whittet (1992) find $A_v/\tau_{9.7} = 18.4 \pm 1$ for many Galactic sources (but not all; the ratio is low in the Galactic Center: Whittet 1992; Gordon et al. 2021). In NGC 5253 the silicate features are strikingly *weak* for the amount of obscuration. D1 has $A_v/\tau_{9.7} \sim 90 \pm 20$, 5 times higher than the Galactic value. D6 lacks silicate absorption, which is consistent with its lower MIR extinction.

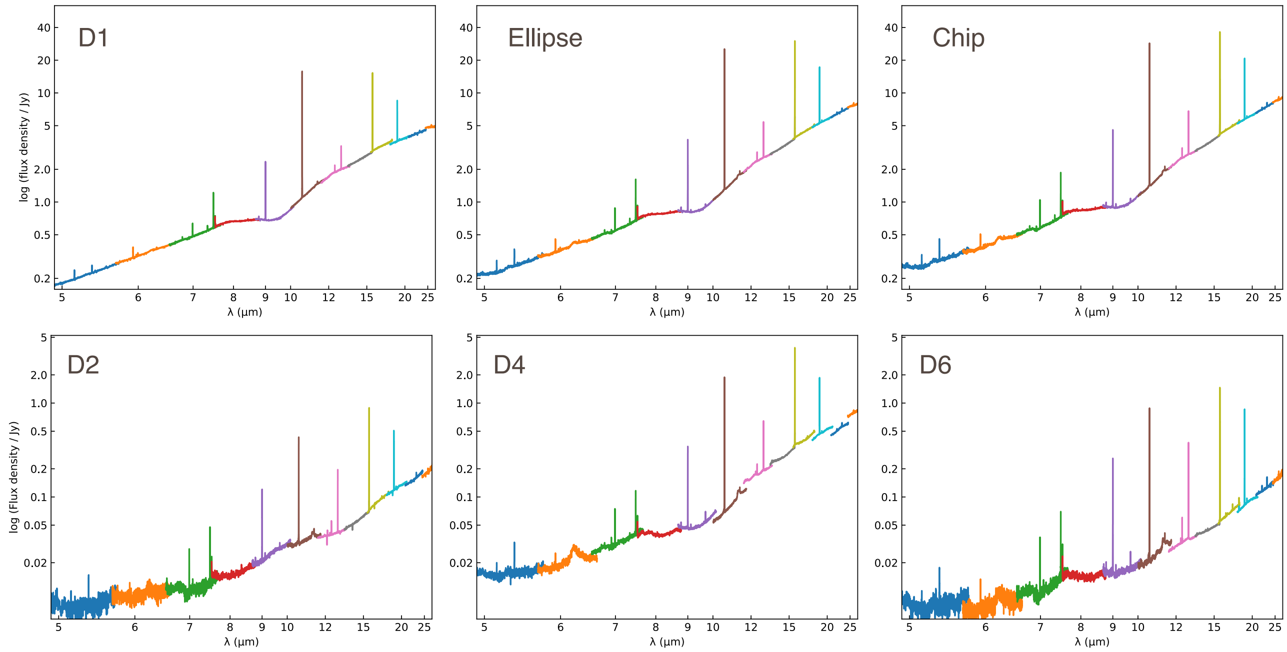

Figure 4. Spectra of the individual regions.

The 9.7μm silicate feature appears in emission in D2. Silicate emission is present in AGB stars and its appearance here may argue that star formation is more evolved in D2 than D1. Silicates are also observed in emission toward the Trapezium (Cesarsky et al. 2000) and source N66 in the LMC (Whelan et al. 2013) where they are attributed to hot dust lying on the near side of the source.

5. FINE STRUCTURE LINES AND NEBULAR CONDITIONS IN THE NGC 5253 STARBURST

In Figure 4 we show the spectra of the sources, displayed on log scales so the full strength of the lines is apparent. Especially important in the mid-infrared are the lines of argon, sulfur, and neon: each element has lines from two different ionization states in this spectral range. The relative strength of the lines depends on the relative abundances of the ions and thus on the hardness of the ionizing spectrum. It is immediately apparent from Figure 4 that the NGC 5253 spectra are dominated by lines of the higher ionization species: [Ne III] 15.5μm (41 eV) and [S IV] 10.5μm (35 eV) are the strongest lines in every source, while [Ne II] 12.8μm (22 eV) is far weaker. [Ar III] 8.99μm (28 eV) is clearly stronger than [Ar II] 6.99μm (16 eV) in every spectrum.

We can compare the MIRI/MRS fluxes to previous ISO and Spitzer measurements with larger apertures. Verma et al. (2003) examined the ISO measurements of mid-infrared emission lines in a dozen starburst galaxies, including NGC 5253. Beirão et al. (2006) presented the Spitzer observations of NGC 5253. The fluxes are generally consistent given that both the ISO and Spitzer apertures are much larger. We compare our fluxes for the Chip region to the Spitzer fluxes, and find that JWST detects 68-72% of the [Ne II] and [Ne III] line fluxes detected by Spitzer and 90-98% for the [S III] and [S IV] lines. Thus the JWST chip seems to pick up nearly all of the sulfur emission in the central 11″x 5″ Spitzer aperture, but only two-thirds of the neon emission, and only one third of the Hu α. These are strong lines, with high signal to noise; even including systematic uncertainties, these differences are significant and suggest that the lines have distinct spatial distributions. With the high spatial resolution of MIRI/MRS, we can investigate these differences.

5.1. *Spatial Distribution of the Fine Structure Lines*

Fine-structure lines of metal ions are the dominant mid-infrared emission lines in H II regions, among the main coolants of the nebulae, and excellent probes of nebular conditions. The JWST spectra on NGC 5253 include lines of neon, argon, sulfur, and some as yet unidentified features.

Figure 5 shows the distribution of the [Ne III] 15.5μm line over the JWST field. Comparison to the 656N and Pfα images shows that the [Ne III] line emission tracks perfectly with the Pfα. Prominent plumes of Hα emission with a full extent of $\sim 100\ pc$, which also appear in the JWST MIRI/MRS Pf α image, suggest a common origin near the central radio source. The origin of the plumes is not clear; are they excited by the deeply embedded radio supernebula core, or by an active ambient radiation field? The high ionization state of the plumes (shown by the [Ne III] emission) suggests that they may be excited by D1 photons that have escaped the high extinction around that source. D2 and D6, luminous H II regions themselves, are more localized sources of [Ne III].

Figure 6 displays the integrated line emission of each of the main fine-structure lines. These images were generated by subtracting a median-averaged continuum from an image of the peak pixel in the wavelength range of the line, a "MOM8" image. For these high dynamic range and spectrally unresolved lines, the MOM8 image is proportional to integrated line intensity. D1 dominates in every line, and D2 and D6 appear as distinct sources. There are definite qualitative differences in spatial distribution between the lower-excitation ([Ar II], [S III] and [Ne II]) and higher-excitation ([Ar III], [S IV], and [Ne III]) lines. The high excitation ions are generally more concentrated onto compact structures such as the H II regions while the low-excitation ions are more extended. South and west of D1, in particular, the low-excitation [S III] and [Ar II] fill in almost the entire chip area. Another difference is the extended emission north and west of D1, the northern "plume" feature, that appears in all the maps, but most clearly in the high-excitation ions. This component of gas also appears in the radio and Hα maps as part of the "plumes".

These features are on too small spatial scales to be seen in the ISO or SPITZER data. The highest spatial resolution measurements in the literature for any of these ions are Gemini/TEXES observations of [S IV] by Beck et al. (2020) with a 0.″3 beam. Those maps show gas extending west and northwest of D1 that Beck et al. (2020) called "arms". These "arms" agree in position and angle with the base of the structure which appears as an elongated "loop" in the current ionic line maps and in the radio continuum of Figure 1, and with a 'plume' appearance in the $H\alpha$ images. The Gemini/TEXES observations did not have the dynamic range to see the full extent of this structure, only the strongest emission close to D1. The TEXES spectra have the advantage of high spectral resolution of 4 km s^{-1}, and found that gas in this western area is blue-shifted by about 30 $km\ s^{-1}$ relative to D1. This suggests strongly that the "loop" is kinematically distinct from the main source and may be an outflow or an expanding ring. This has also been suggested by lower resolution observations (Westmoquette et al. 2013).

Another feature seen in the Gemini/TEXES maps is a distinct source at R.A. 13:39:56.054,-31:38:25.64 Dec. This source also appears in the radio continuum and in the high-excitation ions maps as an emission clump SE of D1, although it can unfortunately be confused in the JWST maps by the "petal" artifact. This clump is kinematically distinct, with an [S IV] line at the same velocity at D1 but with only about half the FWHM. It may be another outflow but its nature is not yet clear.

Keck/NIRSPAO adaptive optics Br α and He I slit spectra of Cohen et al. (2018) see a velocity shift of 13 km/s across the inner 1.″2 core of the supernebula, which they suggest might be due to a bipolar outflow. Both this inner flow and the larger scale shifts seen by Beck et al. (2020) may be related to the large scale plume features that are prominent in the H α image; there are multiple kinematic components seen in H α at higher spatial resolutions that suggest this as well (Monreal-Ibero et al. 2010; Westmoquette et al. 2013).

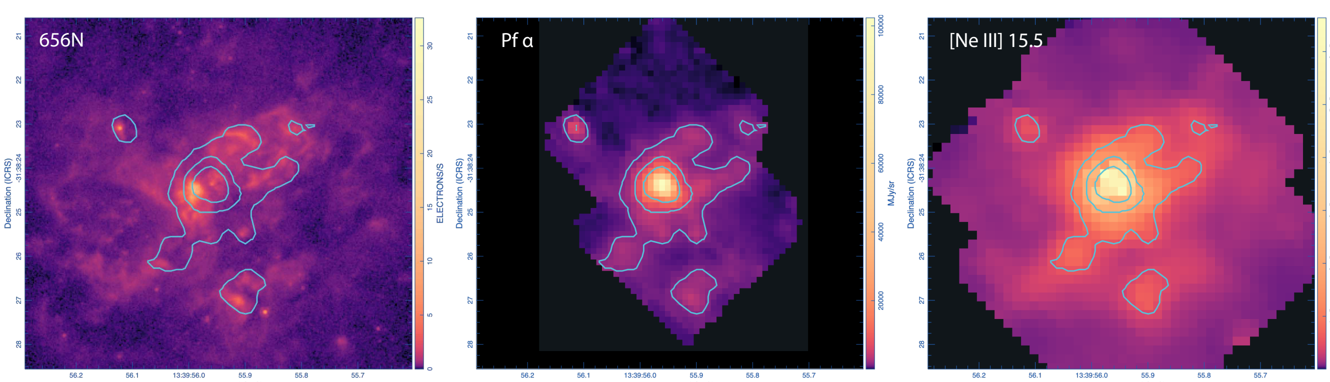

Figure 5. Emission from the giant H II region, NGC 5253-D1. Contours are of Pf α emission, 1.5, 5, 15 GJy/sr. *(Left)* HST 656N image, H α. *(Middle)* Continuum-free line map of Pf α, HI 6-5. *(Right)* Continuum-free line map of [Ne III].

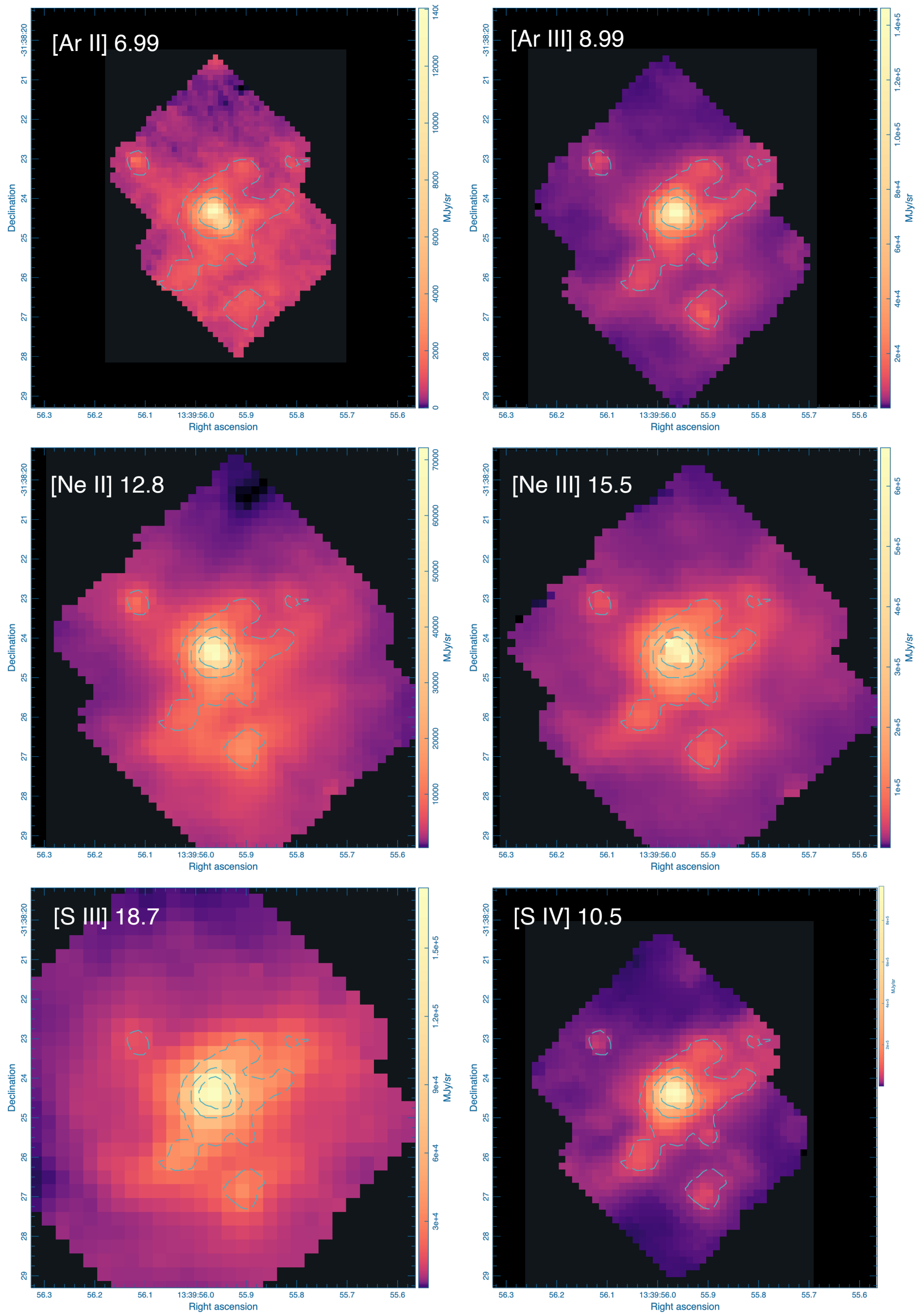

Figure 6. Continuum-free line emission in the iso-elemental lines. Wavelengths in μm are given. Dashed contours are Pf α at a level of 5 GJy/sr to facilitate spatial comparisons. These are MOM8 maps, tracing the peak intensity within the line, so the wedges give intensities, in MJy/sr.

5.2. *Fine structure Line Ratios and Conditions in the Sources*

The three iso-elemental ratios of [Ne III]/[Ne II], [S IV]/[S III], and [Ar III]/[Ar II] are calculated for each of the H II regions and are shown in Table 1. Looking at the chip as a whole, all the ratios are highest for the dominant source D1 (with the exception of sulfur in D2 which is discussed below), decrease to the Ellipse, which covers the plumes, and decrease further to the Whole Chip. This suggests that D1 is the highest excitation and the surrounding regions

Table 3. Isoelemental Lines in NGC 5253

Source	[Ne III]	[Ne II]	[Ne III]/[Ne II]	[S IV]	[S III]	[S IV]/[S III]	[Ar III]	[Ar II]	[Ar III]/[Ar II]
D1	1350	136	9.92	2112	490	4.3	270	25.3	10.67
D2	75.5	14.7	5.13	48.6	38.9	1.3	13.2	2.7	4.88
D4	340	41.1	8.27	221	139	1.6	40.6	6.6	6.15
D6	131	27.7	4.73	94.9	81.3	1.2	27.4	4.7	5.83
Ellipse	2673	301	8.88	3324	1202	2.7	471	56.6	8.30
Chip	3222	409	7.87	3691	1516	2.43	569	78.1	7.3

add lower excitation to the total, diluting the ratios on large scales. This is borne out by the ISO and SPITZER data in larger fields: The neon and sulfur ratios for the Whole Chip agree with Beirão et al. (2006)'s results for the central 27 pc of their dithered Spitzer observations, and ISO with apertures $14 \times 20''$ and larger found lower neon, argon and sulfur ratios $\sim$4.5, $\sim$2.8 and $\sim$1.5, respectively.

It has been established that the excitation ratios of [Ne III]/[Ne II], [S IV]/[S III] and [Ar III]/[Ar II] correlate positively with each other and negatively with the metallicity (Martín-Hernández et al. 2002a; Verma et al. 2003; Wu et al. 2006; Hunt et al. 2010). Beirão et al. (2006) confirmed with Spitzer data that NGC 5253 is in this low metallicity/high-excitation class of starbursts. However, Spitzer was unable to isolate the excitation at resolutions higher than 50 pc; we can here look at sources individually.

D1 is among the highest excitation objects known among Galactic and nearby extragalactic H II regions (Martín-Hernández et al. 2002a; Giveon et al. 2002; Verma et al. 2003; Wu et al. 2006). This is in part because of the low metallicity of NGC 5253, but also because of the extraordinary luminosity of the cluster within D1. The evidence for this comes from the ratios for the lower luminosity H II regions D2, D4 and D6, which are significantly lower in excitation, but are still located in the higher excitation half of Beirão et al. (2006)'s distribution.

In Figure 7 we present maps of the isoelemental line ratios. These maps were constructed by rebinning the continuum-free line images, and convolving ("beam matching") the shorter wavelength line to match the PSF of the longer wavelength. Because of image artifacts, minor features, particularly at the chip edges, must be viewed with caution in these ratio images.

Interpreted broadly, the ratio maps reflect variations in excitation and conditions across the 100 pc central region surrounding D1. The higher excitation line in each ratio peaks near the supernebula core, D1. This is clearest for [Ne III]/[Ne II], ions which have the most straightforward excitation dependence, with excitation energies of 41eV and 22eV respectively.

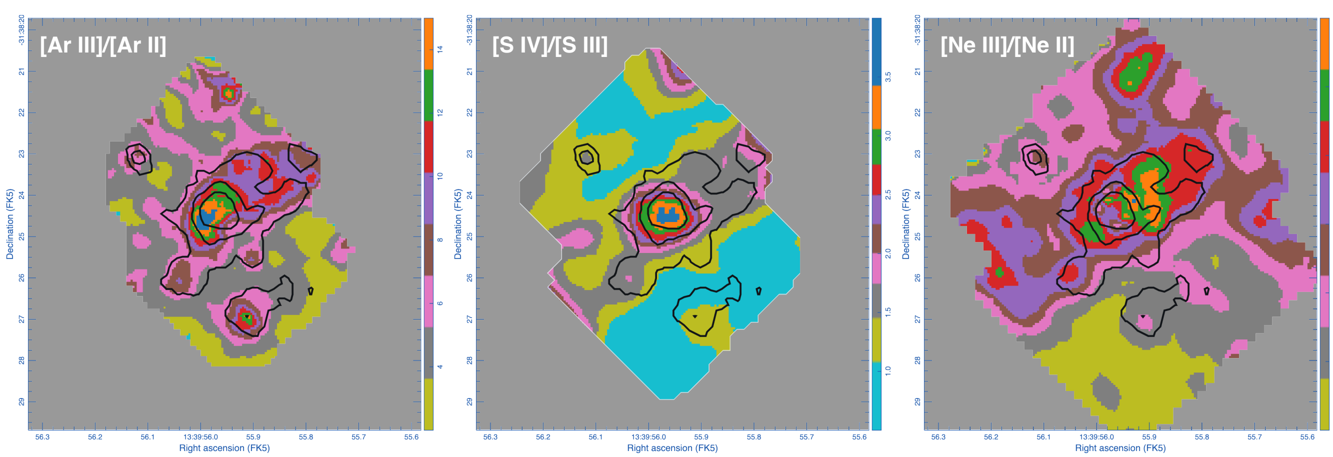

Figure 7. Isoelemental line ratios from continuum-free line emission. The images were convolved to a common PSF before the ratio. Contours are Pf α at 1.2, 3.6, 11 GJy/sr to facilitate spatial comparisons.

[Ar III]/[Ar II] is the lowest excitation pair; the ions are created at 28eV and 16eV, respectively. From the line map of Figure 6 it is clear that the entire region is bathed in [Ar II] emission, while [Ar III] is concentrated in several clumps. The line ratio map shows that [Ar III] favors the H II regions corresponding to D1, D2, and D6, and may also suggest that other H II regions, near the edge of the chip to the north, are influencing the emission. The [Ar III]/[Ar II] ratio is high following plumes traced by Pf α to the north and (slightly) to the south of D1 and is also elevated along other filamentary structures through much of the region.

[S IV] and [S III] have excitation energies of 35eV and 23eV respectively. These lines also have relatively low critical densities and begin to de-excite collisionally at densities above $n_e \sim 10^{4-4.3}$ cm^{-3}. In other words, for densities similar to those of Orion these lines will be suppressed even if the ions have been created by energetic photons. When the ratios are compared with the even higher excitation lines of Ne there is evidence that density is playing a role. The regions of low [S IV] (blue in Fig. 7) can be seen by reference to Fig. 8 to be associated with the dense and warm molecular clouds traced by the strongest CO(3-2) emission. [S IV] is strong along the plumes, as traced clearly by brown in the ratio Fig. 7.

[Ne III]/[Ne II], the highest excitation line pair, peaks at the supernebula core. [Ne III] has the peak line plus continuum intensity of any of the bands, 330 GJy/sr. The line appears to show the push-up/pull-down artifact at the peak on D1, causing the ratio to be suppressed at the peak of the emission, and raised to the north, although this shift of the peak could also be real. (The spectral extraction regions were chosen to be large enough to wash out this artifact among others.) The [Ne III]/[Ne II] ratio is high along the plumes, both northwest and southeast, even though the total ionization is low, indicating the escape of very high energy photons. That this high ratio is seen in the plumes is strong evidence that, in spite of the high extinction in D1, 41eV photons are escaping from the giant cluster within the supernebula core to distances of 50 pc and more.

Full models of the spectra from the NGC 5253 emission regions are now in progress. They will make it possible to determine the nebular and ionization parameters and deduce the stellar populations created by the starburst. A first approach with the models of Rigby & Rieke (2004) may already show the most striking features of the emission regions. Comparing the [Ne III]/[Ne II] and [Ar III]/[Ar II] ratios to Rigby & Rieke (2004)'s low-metallicity models suggests that D1 is very young ($< 3 \times 10^6$ years) and that the upper mass limit for the embedded cluster is at least $50 M_\odot$. D2 and D6 may be consistent with ages up to 5×10^6 years and any mass limit greater than $\sim 40 M_\odot$. D4 appears to be between the conditions of D1 and D2 but must be treated with caution because the fluxes may include emission from D1. NGC 5253 is truly an extreme starburst source.

5.3. *High Excitation Lines*

In the preceding section we showed images of two high excitation lines, [S IV] and [Ne III], with excitation potentials (EP) of 41 eV and 35 eV respectively. They are very strong in D1 and also weakly present in D2 and D6. Other very high excitation lines detected in D1 are [Cl IV] 11.76μm, [O IV] 25.89μm, and [K IV] 5.982μm, which have EP of 40ev, 46eV and 55 eV respectively. Although [O IV] is detected in all regions except D1, [K IV] of similar strength and in a less noisy spectrum, is only detected in D1. We show the image of [K IV] in Figure 8. Because the continuum in D1 is so strong, we checked the continuum subtraction by making a null map by differencing the continuum images on both sides of the line and [K IV] is significantly stronger than the null image.

[O IV] and [K IV] can be created by hot stars with hard radiation fields; they are typically seen in planetary nebulae (Bernard Salas et al. 2001; Jones et al. 2023). The NGC 5253-D1 cluster is not old enough for planetary nebulae to have evolved, but its youth, large stellar population and great compactness make it likely that hot WR stars or stripped stars have formed there.

There are limits to the excitation in NGC 5253-D1. Hernandez et al. (2025) recently detected [Ne V]14.3217μm and [Ne VI] in the starburst center of M83, which is at roughly the same distance as NGC 5253. These lines have very high EP of 97eV and 126 eV respectively. Hernandez et al. (2025) argue that these lines are difficult to excite in star-forming regions, and indeed other regions of M83 have low [Ne III]/[Ne II] ratios, typical of star formation in high metallicity, low excitation H II regions. They thus infer the presence of an AGN in M83. In NGC 5253 we detect a 2σ line near the expected wavelength of [Ne V] with a flux of 2×10^{-18} W m^{-2} in regions D1, Ellipse, and Chip. If this line were [Ne V], its velocity would be blueshifted by 100 km s^{-1} relative to other lines in D1; an offset signifcantly greater than the $\lesssim 30$ km s^{-1} uncertainty of a weak line centroid. The line also appears in measurements of a region, Chip-D1, that includes the entire MIRI/MRS footprint except for D1; the Chip-D1 region is dominated by the lower excitation H II regions, D2 and D6, and diffuse emission. Given the detection in the extended region and the

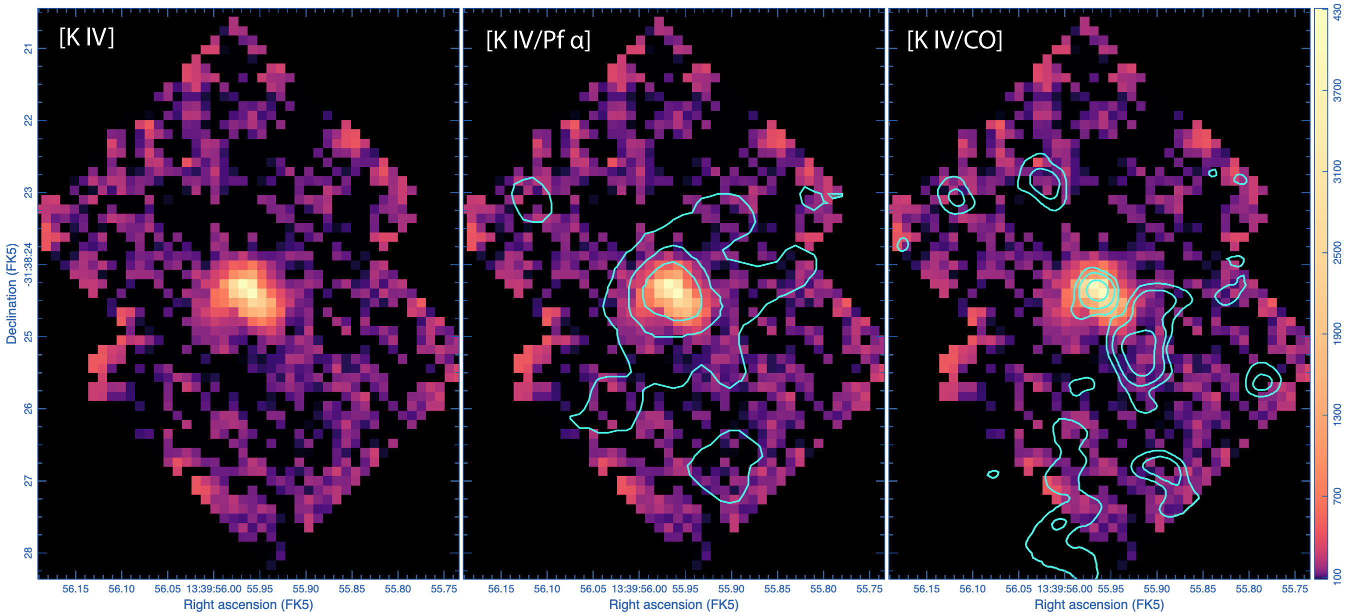

Figure 8. Maximum line intensity (MOM8) map of [K IV], shown with Pfα and CO(3–2) for comparison.

disagreement in redshift, we classify this line as a UIL. [Ne V] 14.3217μm has been detected in an extended region in the dwarf star-forming galaxy I Zw 18 (Hunt et al. 2025; Arroyo-Polonio et al. 2025), but I Zw 18 has a metallicity an order of magnitude less than NGC 5253 and presumably harder radiation fields.

5.4. *Contribution of Mid-Infrared Lines to Total Cooling and Luminosity*

The very bright mid-infrared lines detected by MIRI-MRS contribute to the gas cooling and infrared luminosity within the starburst. In this section we compute the luminosities of the major cooling lines, determine their fractional contribution to the total infrared luminosity, determine which are most important in the individual sources and compare to the far-infrared cooling lines detected in NGC 5253 by Herschel PACS Dwarf Galaxy survey (Cormier et al. 2015; Madden et al. 2013). While Herschel-PACs has a larger beam, 9″ by 12″, it can be compared to the Chip region, which is 6″ by 7″. For most FIR cooling lines, aside perhaps from [C II]157μm, the difference in aperture size is likely insignificant. In most respects, NGC 5253 has the typical far-infrared behaviour of a dwarf galaxy (Cormier et al. 2015), with properties characteristic of high excitation radiation fields and distinct from those of typical star-forming spiral galaxies.

In Table 4 we present the line luminosities, the HI line luminosities, and their relative percentage contributions to the total mid-infrared luminosity, L^{est}_{MIR}, from Paper I. The top six cooling lines in all regions are, in order of importance, [S IV] 10.5, [Ne III] 15.5, [S III] 18.7, [Ar III] 9.0, [Ne II] 12.8 and HI(6-5). In the less luminous regions D2 and D4 [Ne III] dominates and [Ne II] exceeds [Ar III] in luminosity. The top six cooling lines account for $\sim$ 90-93% of the mid-infrared line cooling; the top three lines, [S IV], [Ne III] and [S III] account for 75-83% of total line cooling. HI lines account for about 5% of the line cooling; the most important contributor is Pf$\,\alpha$ (HI (6-5).

Lines contribute $\sim$ 0.4-1.5% to the total mid-infrared luminosity, L_{MIR}, in the different spatial regions. Since we have shown that the Ellipse contains photons escaping from D1, we consider fluxes from Ellipse to be the best measure of the contribution of the massive star cluster within the D1 region. In Ellipse, lines contribute $\sim$ 0.6% to the total luminosity. D6 has the highest line contribution to its MIR luminosity, 1.5%, which may reflect the relatively low extinction of D6. Overall, lines contribute $\sim$ 0.6% of the luminosity in the entire Chip.

One tends to think of line cooling as being dominated by the strong far-infrared lines, but in this starburst region, the mid-infrared contribution to line cooling is significant. The total FIR line cooling for the starburst region is 7.1×10^6 L$_\odot$, based on fluxes from Cormier et al. (2015). The FIR line cooling is dominated by the [C II] 157μm, [O I] 63μm, and

Table 4. Cooling Lines in NGC 5253

Region	L_{MIR}^{est} ($L_\odot$)	L_{MIR}^{HI} ($L_\odot$)	L_{MIR}^{lines} ($L_\odot$)	$\frac{L_{MIR}^{lines}}{L_{MIR}^{est}}$ (%)	$\frac{[S\ IV]}{[Ne\ III]}$
D1	5.5×10^8	1.2×10^5	2.1×10^6	0.38	1.56
D2	1.1×10^7	5.5×10^3	9.4×10^4	0.85	0.64
D4	5.2×10^7	1.4×10^4	3.7×10^5	0.71	0.65
D6	1.2×10^7	8.1×10^3	1.8×10^5	1.5	0.73
Ellipse	6.5×10^8	1.9×10^5	3.8×10^6	0.58	1.24
Chip	7.2×10^8	2.1×10^5	4.4×10^6	0.61	1.2

[O III] 88μm lines. This number can be compared to the mid-infrared contribution, which is $L_{MIR}^{lines} = 4.4 \times 10^6$ $L_\odot$. Hence $\sim$ 38% of the total infrared line cooling of $L_{IR}^{lines} = 1.2 \times 10^7$ $L_\odot$, is from the mid-infrared.

Line cooling contributes only a small fraction of the luminosity in the region. The total infrared luminosity integrated over the SED is $L_{TIR} = 1.4 \times 10^9$ $L_\odot$ (Cormier et al. 2015, corrected to 3.7 Mpc), of which about half is emitted in the $5 - 25\mu$m region. The total line cooling, both mid-infrared and far-infrared for the central 6″ by 7″ region is 1.2×10^7 $L_\odot$. Line cooling represents about 1% of the total infrared luminosity in the Ellipse region; the other 99% of the luminosity is in the dust continuum.

The D1 source has the smallest MIR line luminosity fraction of 0.38%, which reflects its high internal extinction. D1 dominates the luminosity, with more than 40% of L_{TIR} from the starburst due to MIR emission from the 1.″6 D1 region. Based on the observed free-free emission, the predicted Ly α luminosity is 2×10^6 $L_\odot$. If we assume that all the dust continuum emission is hot dust emitting in the mid-infrared from within the H II region, then Ly α heating contributes about 1/3 of the dust luminosity in D1. For the larger Chip region, Ly α dust heating is responsible for $\sim$ 15% of the total infrared luminosity, L_{TIR}.

Silich et al. (2023) considered the contribution to gas heating of turbulence generated by stellar motions within the cluster, as a means of explaining the unusually warm CO (Turner et al. 2015, 2017). From the properties of D1, they compute a turbulent dissipation rate of 0.4-2 $\times 10^4$ $L_\odot$. This turbulence will affect both ionized and neutral gas; the neutral gas cooling will be dominated by the FIR lines. Cooling by ionized gas appears to dominate in D1, with $L_{ionized} \sim 6 \times 10^6$ $L_\odot$ or $\sim$ 1% of the total MIR luminosity of D1, even not including any contribution from [C II] 157μm. The ionized gas cooling exceeds the turbulent heating by two orders of magnitude. Therefore, not surprisingly, the temperature of the gas in the H II region is determined by radiative heating.

5.5. *Elemental Abundances in the NGC 5253 Starburst*

Following Giveon et al. (2002) we address elemental abundances relative to hydrogren by comparing the infrared fine-structure lines to an infrared HI line. Our reference line is Pfα, the strongest HI line in the JWST spectra. The following equations were used:

$$\frac{[\mathrm{Ne}]}{[\mathrm{H}]} = 1.658 \times 10^{-6} \times \frac{2.30 f_{Ne\,II} + f_{Ne\,III}}{f_{Pf\alpha}}$$

$$\frac{[\mathrm{Ar}]}{[\mathrm{H}]} = 2.203 \times 10^{-7} \times \frac{f_{Ar\,II} + 1.26 f_{Ar\,III}}{f_{Pf\alpha}}$$

We do not apply an ionization correction factor, since charge-exchange reactions reduce the Ar IV population, limiting higher ionization argon, and Ne IV has such a high excitation potential that it is unlikely to be excited. Both pairs of lines have reasonably high critical densities above 10^5 cm^{-3}. We do not include sulfur because its critical densities are so low that collisional deexcitation is probable at the densities inferred from radio free-free and CO excitation in NGC 5253. Table 5 shows the abundances thus derived for all the sources. Based on the photometric accuracy of a few percent, we estimate the uncertainties in the 12+log[X]/[H] to be 0.01 for Ne and 0.02-0.03 for Ar.

The abundances of Ne and Ar are fairly consistent across the regions. Ne is the most deviant: it is is slightly underabundant, by 0.7, in D1 and overabundant by 1.7 in D4. Ar is also slightly less abundant in D1, but within the uncertainties. We have previously noted that the [Ne III] line is by far the strongest in the spectra and is associated with clear artifacts affecting both D1 and D4, so we hesitate to interpret these abundance variations.

Table 5. Abundances in NGC 5253

	D1	D2	D4	D6	Ellipse	Chip
12+log [Ne]/[H]	7.41	7.57	7.81	7.64	7.55	7.57
12+log [Ar]/[H]	5.87	5.94	6.06	6.07	5.96	5.98

Note—For each element the table shows the standard format 12 plus the log10 of the relative abundance of the element.

We compare to solar values as given in Lodders (2021), and find that the solar abundance of neon is 12+log([Ne]/[H]) = 8.15 and that of argon is 12+log([Ar]/[H]) = 6.5. From these values, we infer that the metallicity of NGC 5253 is 0.28 $Z_{\odot}$ for Ne and 0.32 $Z_{\odot}$ for Ar. These values are consistent with what has been determined based on other nebular lines in the region (Walsh & Roy 1989; Kobulnicky et al. 1997; Westmoquette et al. 2013).

5.6. *A mystery feature*

An unidentified feature is seen on and close to D2. It combines emission from $14.00 - 14.02\mu m$ with absorption between $13.969 - 13.99\mu m$. The width and shape of both emission and absorption features strongly suggests that they arise in a molecular band or bands. Many common interstellar molecules, most dominated by HCN, have bands around $14\mu m$ that could contribute to a broad line feature. The combination of emission with blue-shifted absorption can be caused by an extended outflow. If this is the mechanism on D2 it implies a velocity range of $300 - 600kms^{-1}$, consistent with stellar outflows. Further study of D2 could determine the evolutionary state of those sources and trace the progress of star formation in this starburst.

6. DISCUSSION

The goals of this project included characterizing star forming regions in the center of NGC 5253 and determining how the massive central cluster D1 affects its surroundings. The JWST MIRI/MRS observations agree with earlier ISO and Spitzer results that NGC 5253 is a very high excitation source. Ratios of [Ne III]/[Ne II] exceed 5-8 in all the H II regions and are 10 in D1, the aperture containing the massive cluster. This is one of the highest values of [Ne III]/[Ne II] seen in any starburst galaxy (Martín-Hernández et al. 2002b; Verma et al. 2003; Wu et al. 2006), larger even than the LMC plantary nebula SMP LMC 058 (Jones et al. 2023). The ratio of [S IV]/[S III] is also highest in D1, giving a value of 4.3, as compared to 1.2-1.6 for the other H II regions. The line ratios of the H II regions other than D1 resemble those of other low metallicity star formation regions; the excitation of D1 is extreme, consistent with very massive and very young stars.

We have shown that obscuration is high around the D1 cluster, with mid-infrared extinction $A(MIR) \sim 1.4$ consistent with 35 magnitudes of visual extinction. In spite of this high extinction, JWST MIRI/MRS shows that UV photons escape from D1. In Paper I, we found that roughly 25% of the mid-infrared and radio free-free luminosity appeared to be emitted beyond the D1 aperture. The MIRI/MRS imaging confirms that D1 is the source of the photons: the "plumes" seen in Hα images are also reflected in regions of high [Ne III]/[Ne II] ratio (Fig. 7). Thus 50 eV photons from D1 reach distances of at least 50-60 pc from D1 in spite of the heavy extinction. This is another indication that, as suggested by CO (Turner et al. 2017; Consiglio et al. 2017), the molecular cloud in the D1 core complex has a highly clumped and porous structure that creates paths for photon escape.

The kinematic picture in this region is extremely complex. However, it is consistent with the turbulent model of the molecular core (Silich et al. 2023) that suggests that massive stars moving in the gravitational well of a dense star cluster will continuously stir the molecular gas, compensating for dissipation by turbulence and supporting a quasi-equilibrium state. Stellar winds and ionization fronts around the moving stars create cavities and tunnels which will expand into the lower density regions close to the cloud edge; some cavities may break out of the cloud completely and allow the ionizing photons to escape.

Not only a porous cloud structure but active wind dynamics may be at work here, as suggested by ground-based spectroscopy which detects a shift from red to blue across the supernebula from southeast to northwest (Westmoquette et al. 2013; Cohen et al. 2018; Beck et al. 2020), of order 13-30 km s^{-1}. The linewidth of the supernebula core in Br α is 65 km s^{-1}, but with a weak plateau feature extending to 150 km s^{-1}. H α line profiles, which because of extinction must arise from a larger area, suggest that in addition to narrow line features with shifts of 40 km s^{-1}, there are also broad components (Monreal-Ibero et al. 2010; Westmoquette et al. 2013). These flows would have to be reconciled with the relatively placid CO gas of the D1 molecular cloud, whose 25 $\mathrm{km\,s^{-1}}$ linewidth is completely dominated by the stellar orbits within D1 (Turner et al. 2017). It is clear that the kinematic picture in this region is extremely complex.

Photon escape may also explain how optical and UV tracers of Wolf-Rayet stars are seen even from this highly obscured region. (Conti 1991; Schaerer et al. 1997). GMOS-IFU observations of Westmoquette et al. (2013) detect a "red WR bump" spectral feature at 0.5765-0.5875 μm. Their image shows that the red WR bump appears to spatially coincide with D2 and D6 and with a "plume" north of D1. Although D6 has lower MIR extinction than the other H II regions, D2 has high MIR extinction, and the detection of WR features there may also indicate porosity. The WR feature in the northern "plume" almost certainly originates in D1 and has escaped through the clumpy and porous gas there. Thus the spectroscopic signatures of WR stars can provide important clues to the stellar content of these embedded clusters in spite of the very high visual obscuration.

7. CONCLUSIONS

We have presented here an overview of the rich emission line spectrum measured by JWST for the starburst in NGC 5253 to follow on a study of the continuum sources presented in Paper I (Turner et al. 2025). We present fluxes and velocities for more than 70 lines, measured in six different apertures, including the supernebula core, NGC 5253-D1, and three other H II regions and mid-infrared continuum sources, NGC 5253-D2, NGC 5253-D4, and NGC 5253-D6. We have derived the extinction law and total obscuration based on 30 HI lines detected from four different series. From the fluxes of the strong fine structure lines of [Ar II] 6.99, [Ar III] 8.99, [Ne II] 12.8, [Ne III] 15.5, [SIII] 18.7, and [SIV] 10.5 we made 'first pass' estimates of conditions in the 4 embedded HII regions, including the supernebula D1 and the less luminous D2, D4 and D6 regions that were defined in Paper 1. We find:

- The extinction derived from ratios of HI recombination lines and the free-free radio continuum is almost flat from 5-20 microns, as it is in the Galaxy.
- The extinctions for the different regions can be significant, even in the mid-infrared. Extinctions derived for the H II regions are: A(MIR) $= 1.4 \pm 0.2$ for D1 (supernebula core), 0.7 ± 0.2 for D2, and 0 ± 0.2 for D4 and D6. These correspond to visual extinctions of Av = 35 magnitudes for D1, 18 magnitudes for D2, and could be as high as 5 magnitudes for D4 and D6, although they are also consistent with zero visual extinction.
- The Galactic relation between A_v and the depth of the silicate feature $\tau_{9.7}$ does not hold; the silicate feature on D1 is weaker than predicted by factors ~ 5.
- The isoelemental line ratios, particularly [Ne III]/[Ne II], as well as the detection of [K IV] 5.98μm and [O IV] 25.89μm show that the embedded cluster source D1 has extremely high excitation, consistent with very massive ($\sim 100 M_\odot$) stars at very young ages. This demonstrates that the high ratios in D1 are in part due to a large young stellar population ($L \sim 10^9\ L_\odot$) within the $r \sim 1-2$ pc supernebula core, but in part also due to the low metallicity of the galaxy, since the smaller ($L \sim 10^7\ \mathrm{L_\odot}$) H II regions also have high excitation.
- We compute a total cooling rate from the MIR lines of $4.4 \times 10^6\ \mathrm{L_\odot}$, about half the cooling rate from the FIR lines (Cormier et al. 2015), so MIR lines are significant contributors to cooling. The MIR lines contribute $\sim$ 0.4-1.5% of the mid-infrared luminosity in the different regions.
- We compute abundances for neon, 12 + log([Ne]/[H]) = 7.4-7.8, and argon, 12 + log([Ne]/[H]) = 5.9-6.1. We do not see notable spatial trends; the D1 abundances tend to be slightly low, but within the uncertainties. These values are consistent with previous work showing that the nebular metallicity of NGC 5253 is $\sim 0.3\ Z_\odot$.
- Images of the isoelemental line ratios show that photons with energies as high as 46 eV are escaping the D1 supernebula core and reaching distances of at least 50 pc from the cluster, in spite of the very high ($\mathrm{A_v} \sim 35$) visual extinction. Based on the distribution of free-free emission, we estimate that $\gtrsim$25% of the photons escape D1 (Turner et al. 2025). This, with evidence of clumpiness in the CO (Turner et al. 2017; Consiglio et al. 2017) suggests that the interior of this deeply embedded cloud/cluster is clumpy and porous, and allows shorter wavelength spectroscopic signatures, such as WR features, to be seen.

ACKNOWLEDGMENTS

We thank the JWST Help Desk for their substantial assistance with the data.

Facilities: JWST(MIRI-MRS), IRSA, NED, ALMA

Software: astropy (Astropy Collaboration et al. 2013, 2018, 2022), R (R Core Team 2023), Cloudy (Ferland et al. 2017), jdaviz (Developers et al. 2025), CARTA (Comrie et al. 2025), AIPS (Greisen 1990)

DATA AVAILABILITY

JWST data used in this paper can be found in MAST: 10.17909/9mwc-xk11

REFERENCES

Alonso-Herrero, A., Takagi, T., Baker, A. J., et al. 2004, ApJ, 612, 222, doi: 10.1086/422448

Argyriou, I., Glasse, A., Law, D. R., et al. 2023a, A&A, 675, A111, doi: 10.1051/0004-6361/202346489

Argyriou, I., Lage, C., Rieke, G. H., et al. 2023b, A&A, 680, A96, doi: 10.1051/0004-6361/202346490

Arroyo-Polonio, A., Kehrig, C., Vílchez, J. M., et al. 2025, ApJL, 987, L36, doi: 10.3847/2041-8213/ade874

Astropy Collaboration, Robitaille, T. P., Tollerud, E. J., et al. 2013, A&A, 558, A33, doi: 10.1051/0004-6361/201322068

Astropy Collaboration, Price-Whelan, A. M., Sipőcz, B. M., et al. 2018, AJ, 156, 123, doi: 10.3847/1538-3881/aabc4f

Astropy Collaboration, Price-Whelan, A. M., Lim, P. L., et al. 2022, ApJ, 935, 167, doi: 10.3847/1538-4357/ac7c74

Beck, S. C., Lacy, J., Turner, J., et al. 2020, MNRAS, 497, 1675, doi: 10.1093/mnras/staa1819

Beck, S. C., Turner, J. L., Ho, P. T. P., Lacy, J. H., & Kelly, D. M. 1996, ApJ, 457, 610, doi: 10.1086/176757

Beirão, P., Brandl, B. R., Devost, D., et al. 2006, ApJL, 643, L1, doi: 10.1086/505027

Bendo, G. J., Miura, R. E., Espada, D., et al. 2017, MNRAS, 472, 1239, doi: 10.1093/mnras/stx1837

Bergin, E. A., Alves, J., Huard, T., & Lada, C. J. 2002, ApJL, 570, L101, doi: 10.1086/340950

Bernard Salas, J., Pottasch, S. R., Beintema, D. A., & Wesselius, P. R. 2001, A&A, 367, 949, doi: 10.1051/0004-6361:20000435

Calzetti, D., Meurer, G. R., Bohlin, R. C., et al. 1997, AJ, 114, 1834, doi: 10.1086/118609

Calzetti, D., Johnson, K. E., Adamo, A., et al. 2015, ApJ, 811, 75, doi: 10.1088/0004-637X/811/2/75

Cesarsky, D., Jones, A. P., Lequeux, J., & Verstraete, L. 2000, A&A, 358, 708, doi: 10.48550/arXiv.astro-ph/0002282

Chiar, J. E., & Tielens, A. G. G. M. 2006, ApJ, 637, 774, doi: 10.1086/498406

Cohen, D. P., Turner, J. L., Consiglio, S. M., Martin, E. C., & Beck, S. C. 2018, ApJ, 860, 47, doi: 10.3847/1538-4357/aac170

Comrie, A., Wang, K.-S., Hwang, Y.-H., et al. 2025, CARTA: The Cube Analysis and Rendering Tool for Astronomy, 5.0, Zenodo, doi: 10.5281/zenodo.17050846

Consiglio, S. M., Turner, J. L., Beck, S., et al. 2017, ApJ, 850, 54, doi: 10.3847/1538-4357/aa93dc

Conti, P. S. 1991, ApJ, 377, 115, doi: 10.1086/170340

Cormier, D., Madden, S. C., Lebouteiller, V., et al. 2015, A&A, 578, A53, doi: 10.1051/0004-6361/201425207

Decleir, M., Gordon, K. D., Andrews, J. E., et al. 2022, ApJ, 930, 15, doi: 10.3847/1538-4357/ac5dbe

Developers, J., Averbukh, J., Bradley, L., et al. 2025, Jdaviz, v4.4.1, Zenodo, doi: 10.5281/zenodo.17211099

Dicken, D., Marín, M. G., Shivaei, I., et al. 2024, A&A, 689, A5, doi: 10.1051/0004-6361/202449451

Draine, B. T. 2011a, Physics of the Interstellar and Intergalactic Medium (Princeton University Press)

—. 2011b, ApJ, 732, 100, doi: 10.1088/0004-637X/732/2/100

Ferland, G. J., Chatzikos, M., Guzmán, F., et al. 2017, RMxAA, 53, 385, doi: 10.48550/arXiv.1705.10877

Gáspár, A., Rieke, G. H., Guillard, P., et al. 2021, PASP, 133, 014504, doi: 10.1088/1538-3873/abcd04

Giveon, U., Sternberg, A., Lutz, D., Feuchtgruber, H., & Pauldrach, A. W. A. 2002, ApJ, 566, 880, doi: 10.1086/338125

Gordon, K. D., Clayton, G. C., Decleir, M., et al. 2023, ApJ, 950, 86, doi: 10.3847/1538-4357/accb59

Gordon, K. D., Misselt, K. A., Bouwman, J., et al. 2021, ApJ, 916, 33, doi: 10.3847/1538-4357/ac00b7

Greisen, E. W. 1990, in Acquisition, Processing and Archiving of Astronomical Images, 125–142

Guseva, N. G., Izotov, Y. I., Stasińska, G., et al. 2011, A&A, 529, A149, doi: 10.1051/0004-6361/201016291

Harris, J., Calzetti, D., Gallagher, John S., I., Smith, D. A., & Conselice, C. J. 2004, ApJ, 603, 503, doi: 10.1086/381669

Hernandez, S., Smith, L. J., Jones, L. H., et al. 2025, ApJ, 983, 154, doi: 10.3847/1538-4357/adba5d

Hunt, L. K., Thuan, T. X., Izotov, Y. I., & Sauvage, M. 2010, ApJ, 712, 164, doi: 10.1088/0004-637X/712/1/164

Hunt, L. K., Aloisi, A., Navarro, M. G., et al. 2025, ApJ, 992, 48, doi: 10.3847/1538-4357/adfb69

Indebetouw, R., Mathis, J. S., Babler, B. L., et al. 2005, ApJ, 619, 931, doi: 10.1086/426679

Jones, O. C., Álvarez-Márquez, J., Sloan, G. C., et al. 2023, MNRAS, 523, 2519, doi: 10.1093/mnras/stad1609

Kobulnicky, H. A., Skillman, E. D., Roy, J.-R., Walsh, J. R., & Rosa, M. R. 1997, ApJ, 477, 679, doi: 10.1086/303742

Lai, T. S. Y., Smith, J. D. T., Peeters, E., et al. 2024, ApJ, 967, 83, doi: 10.3847/1538-4357/ad354b

Lai, T. S. Y., Duval, S., Smith, J. D. T., et al. 2025, arXiv e-prints, arXiv:2509.04662, doi: 10.48550/arXiv.2509.04662

Law, D. R., E. Morrison, J., Argyriou, I., et al. 2023, AJ, 166, 45, doi: 10.3847/1538-3881/acdddc

Lebofsky, M. J., & Rieke, G. H. 1979, ApJ, 229, 111, doi: 10.1086/156934

Lodders, K. 2021, SSRv, 217, 44, doi: 10.1007/s11214-021-00825-8

López-Sánchez, Á. R., Esteban, C., García-Rojas, J., Peimbert, M., & Rodríguez, M. 2007, ApJ, 656, 168, doi: 10.1086/510112

Lutz, D., Kunze, D., Spoon, H. W. W., & Thornley, M. D. 1998, A&A, 333, L75, doi: 10.48550/arXiv.astro-ph/9803314

Lutz, D., Feuchtgruber, H., Genzel, R., et al. 1996, A&A, 315, L269

Madden, S. C., Rémy-Ruyer, A., Galametz, M., et al. 2013, PASP, 125, 600, doi: 10.1086/671138

Martín-Hernández, N. L., Schaerer, D., & Sauvage, M. 2005, A&A, 429, 449, doi: 10.1051/0004-6361:20041603

Martín-Hernández, N. L., Vermeij, R., Tielens, A. G. G. M., van der Hulst, J. M., & Peeters, E. 2002a, A&A, 389, 286, doi: 10.1051/0004-6361:20020528

Martín-Hernández, N. L., Peeters, E., Morisset, C., et al. 2002b, A&A, 381, 606, doi: 10.1051/0004-6361:20011504

Meier, D. S., Turner, J. L., & Beck, S. C. 2002, AJ, 124, 877, doi: 10.1086/341752

Monreal-Ibero, A., Vílchez, J. M., Walsh, J. R., & Muñoz-Tuñón, C. 2010, A&A, 517, A27, doi: 10.1051/0004-6361/201014154

Monreal-Ibero, A., Walsh, J. R., & Vílchez, J. M. 2012, A&A, 544, A60, doi: 10.1051/0004-6361/201219543

Natta, A., & Panagia, N. 1984, ApJ, 287, 228, doi: 10.1086/162681

Pineda, J. L., Goldsmith, P. F., Chapman, N., et al. 2010, ApJ, 721, 686, doi: 10.1088/0004-637X/721/1/686

R Core Team. 2023, R: A Language and Environment for Statistical Computing, R Foundation for Statistical Computing, Vienna, Austria. https://www.R-project.org/

Rigby, J. R., & Rieke, G. H. 2004, ApJ, 606, 237, doi: 10.1086/382776

Rodríguez-Rico, C. A., Goss, W. M., Turner, J. L., & Gómez, Y. 2007, ApJ, 670, 295, doi: 10.1086/520709

Schaerer, D., Contini, T., Kunth, D., & Meynet, G. 1997, ApJL, 481, L75, doi: 10.1086/310659

Silich, S., Turner, J., Mackey, J., & Martínez-González, S. 2023, ApJL, 944, L32, doi: 10.3847/2041-8213/acb687

Smith, J. D. T., Draine, B. T., Dale, D. A., et al. 2007, ApJ, 656, 770, doi: 10.1086/510549

Smith, L. J., Bajaj, V., Ryon, J., & Sabbi, E. 2020, ApJ, 896, 84, doi: 10.3847/1538-4357/ab8f94

Spoon, H. W. W., Marshall, J. A., Houck, J. R., et al. 2007, ApJL, 654, L49, doi: 10.1086/511268

Storey, P. J., & Hummer, D. G. 1995, MNRAS, 272, 41, doi: 10.1093/mnras/272.1.41

Turner, J. L., & Beck, S. C. 2004, ApJL, 602, L85, doi: 10.1086/382699

Turner, J. L., Beck, S. C., Benford, D. J., et al. 2015, Nature, 519, 331, doi: 10.1038/nature14218

Turner, J. L., Beck, S. C., Crosthwaite, L. P., et al. 2003, Nature, 423, 621, doi: 10.1038/nature01689

Turner, J. L., Consiglio, S. M., Beck, S. C., et al. 2017, ApJ, 846, 73, doi: 10.3847/1538-4357/aa8669

Turner, J. L., Ho, P. T. P., & Beck, S. C. 1998, AJ, 116, 1212, doi: 10.1086/300485

Turner, J. L., Beck, S. C., Zweig, E. A., et al. 2025

Verma, A., Lutz, D., Sturm, E., et al. 2003, A&A, 403, 829, doi: 10.1051/0004-6361:20030408

Walsh, J. R., & Roy, J.-R. 1989, MNRAS, 239, 297, doi: 10.1093/mnras/239.2.297

Westmoquette, M. S., James, B., Monreal-Ibero, A., & Walsh, J. R. 2013, A&A, 550, A88, doi: 10.1051/0004-6361/201220580

Whelan, D. G., Lebouteiller, V., Galliano, F., et al. 2013, ApJ, 771, 16, doi: 10.1088/0004-637X/771/1/16

Whittet, D. C. B. 1992, Dust in the galactic environment (IOP Publishing)

Wu, Y., Charmandaris, V., Hao, L., et al. 2006, ApJ, 639, 157,
doi: 10.1086/49922610.48550/arXiv.astro-ph/0510856